



UNIVERSIDAD DE INVESTIGACIÓN DE TECNOLOGÍA EXPERIMENTAL YACHAY

Escuela de Ciencias Biológicas e Ingeniería

TÍTULO:

Physicochemical characterization of biopolymer extracted from the biodiversity of Ecuador as potential adsorbent for removal of heavy metals ions from wastewater.

Trabajo de integración curricular presentado como requisito para la obtención del título de Ingeniero Biomédico

Autor:

Jhonny Israel Caicho Caranqui

Tutor:

PhD. Lenin Ramirez

Co-tutor:

PhD. Frank Alexis

PhD. Julio Chacón

Urcuquí, marzo 2022

Urququí, 8 de agosto de 2022

SECRETARÍA GENERAL
ESCUELA DE CIENCIAS BIOLÓGICAS E INGENIERÍA
CARRERA DE BIOMEDICINA
ACTA DE DEFENSA No. UITEY-BIO-2022-00018-AD

En la ciudad de San Miguel de Urququí, Provincia de Imbabura, a los 8 días del mes de agosto de 2022, a las 10:30 horas, en el Aula S_CAN de la Universidad de Investigación de Tecnología Experimental Yachay y ante el Tribunal Calificador, integrado por los docentes:

Presidente Tribunal de Defensa Dr. CASTILLO MORALES, JOSE ANTONIO , Ph.D.
Miembro No Tutor DAVALOS MONTEIRO, RAUL LEANDRO , Ph.D.
Tutor Dr. RAMIREZ CANDO, LENIN JAVIER , Ph.D.

Se presenta el(la) señor(ita) estudiante **CAICHO CARANQUI, JHONNY ISRAEL**, con cédula de identidad No. **0605564103**, de la **ESCUELA DE CIENCIAS BIOLÓGICAS E INGENIERÍA**, de la Carrera de **BIOMEDICINA**, aprobada por el Consejo de Educación Superior (CES), mediante Resolución **RPC-SO-43-No.496-2014**, con el objeto de rendir la sustentación de su trabajo de titulación denominado: **Physicochemical characterization of biopolymer extracted from the biodiversity of Ecuador as potential adsorbent for removal of heavy metals ions from wastewater.**, previa a la obtención del título de **INGENIERO/A BIOMÉDICO/A**.

El citado trabajo de titulación, fue debidamente aprobado por el(los) docente(s):

Tutor Dr. RAMIREZ CANDO, LENIN JAVIER , Ph.D.
Co - Tutor Dr. CHACON TORRES, JULIO CESAR , Ph.D.
Co - Tutor (Externo) Dr. ALEXIS FRANK , Ph.D.

Y recibió las observaciones de los otros miembros del Tribunal Calificador, las mismas que han sido incorporadas por el(la) estudiante.

Previamente cumplidos los requisitos legales y reglamentarios, el trabajo de titulación fue sustentado por el(la) estudiante y examinado por los miembros del Tribunal Calificador. Escuchada la sustentación del trabajo de titulación, que integró la exposición de el(la) estudiante sobre el contenido de la misma y las preguntas formuladas por los miembros del Tribunal, se califica la sustentación del trabajo de titulación con las siguientes calificaciones:

Tipo	Docente	Calificación
Miembro Tribunal De Defensa	DAVALOS MONTEIRO, RAUL LEANDRO , Ph.D.	10,0
Presidente Tribunal De Defensa	Dr. CASTILLO MORALES, JOSE ANTONIO , Ph.D.	10,0
Tutor	Dr. RAMIREZ CANDO, LENIN JAVIER , Ph.D.	10,0

Lo que da un promedio de: **10 (Diez punto Cero)**, sobre 10 (diez), equivalente a: **APROBADO**

Para constancia de lo actuado, firman los miembros del Tribunal Calificador, el/la estudiante y el/la secretario ad-hoc.



CAICHO CARANQUI, JHONNY ISRAEL
Estudiante



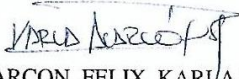
Dr. CASTILLO MORALES, JOSE ANTONIO , Ph.D.
Presidente Tribunal de Defensa



Dr. RAMIREZ CANDO, LENIN JAVIER , Ph.D.
Tutor



DAVALOS MONTEIRO, RAUL LEANDRO , Ph.D.
Miembro No Tutor

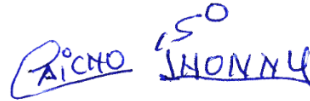


ALARCON FELIX, KARLA ESTEFANIA
Secretario Ad-hoc

AUTORÍA

Yo, **JHONNY ISRAEL CAICHO CARANQUI**, con cédula de identidad **0605564103**, declaro que las ideas, juicios, valoraciones, interpretaciones, consultas bibliográficas, definiciones y conceptualizaciones expuestas en el presente trabajo; así cómo, los procedimientos y herramientas utilizadas en la investigación, son de absoluta responsabilidad de el/la autora (a) del trabajo de integración curricular. Así mismo, me acojo a los reglamentos internos de la Universidad de Investigación de Tecnología Experimental Yachay.

Urququí, agosto 2022.



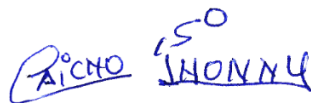
Jhonny Israel Caicho Caranqui
CI: 0605564103

AUTORIZACIÓN DE PUBLICACIÓN

Yo, **JHONNY ISRAEL CAICHO CARANQUI**, con cédula de identidad **0605564103**, cedo a la Universidad de Investigación de Tecnología Experimental Yachay, los derechos de publicación de la presente obra, sin que deba haber un reconocimiento económico por este concepto. Declaro además que el texto del presente trabajo de titulación no podrá ser cedido a ninguna empresa editorial para su publicación u otros fines, sin contar previamente con la autorización escrita de la Universidad.

Asimismo, autorizo a la Universidad que realice la digitalización y publicación de este trabajo de integración curricular en el repositorio virtual, de conformidad a lo dispuesto en el Art. 144 de la Ley Orgánica de Educación Superior.

Urcuquí, agosto 2022.



Jhonny Israel Caicho Caranqui
CI: 0605564103

Dedication

*To my mother Mariana, my father José, and my whole family for their
love, patience, and unconditional support.*

*To my brothers, Juan, Elsa, Nelson, David, Marcia, Vilma, for the
motivation not to give up, Vero, Lidia, and Karina and my aunt Petrona.*

To my nephews Jahir, Bryan, Connie, and my pretty Emmy.

To all my professors during my career.

*To all the scientists, and I hope this work helps us build green technology
for the benefit of humanity and the planet one day.*

Jhonny Israel Caicho Caranqui

Acknowledgments

When I started this journey, I was uncertain if I would make it. After years, I am writing these lines as a tribute and eternal gratitude to all those who were part of it and motivated me to continue, starting with my parents for their great sacrifice and my family to be attentive during these years of my university career. Any achievement or success that awaits me in the future is because of and for them.

I thank Yachay Tech University and all the spectacular professors I had who shared their knowledge and were part of my education as a Biomedical Engineer. To each of them, I owe the tools learned. (Frank, Nelson, Si Amar, Santiago, Diego, Lenin, Graciela, Fernando, Raúl, Jose, Eduardo, Hugo, Juan)

Thanks my tutor Frank Alexis for being a teacher, friend, and inspiration. I admire his passion for biomaterials, scientist and reiterate that work should not remain written but materialize, and Lenin Ramirez for his guidance in developing this research project.

I want to thank all my friends and colleagues (Bryan, Carlos, Oscar, Steven, Erick, Byron, Esteban, Gaby, Lisbeth, Nicole, Juan, Andre, Cata) for sharing amazing adventures on and off-campus. To Cesar that since school, he has been motivating me. To Cristina P and Cinthya, who arrived just in time.

To Cristina C for her support; she has been my life partner and making my days less complicated during this journey and teaching me what the feeling called love is all about. You came less expected to change. I wish you health, well-being, success and happiness wherever you are.

To the School of Biological Sciences and Chemical Sciences for allowing the use of the laboratories. To professors Lola, Floralba, Manuel, Alicia, and Paola for their help accessing the laboratory. To Edward for the support in the XRD data collection and SENESCYT-INETA (grant PIC-18-INE-YACHAY-001) for the financial support in the acquisition of the Rigaku diffractometer equipment. As well as Elizabeth for the help in capturing SEM and EDX images. To the professor of the EPN Victor for the collaboration in taking measurements of TGA and BET. To professors Sudip and Sebastiano from University of Calabria for the opportunity internship and to be part of their laboratory learning about experimental science.

Finally, thank to you, the readers that follow my journey.

Jhonny Israel Caicho Caranqui

Resumen

El agua contaminada por metales pesados de diversas fuentes antropogénicas es una gran preocupación en la comunidad mundial, debido a su impacto en el ser humano y medios acuáticos. Los materiales adsorbentes a base de celulosa son de gran interés por su característica biodegradable y no tóxica. Entre los métodos de tratamiento de agua, la adsorción es de gran importancia por ser un proceso simple, de bajo costo y ser una tecnología alternativa sostenible para remover trazas de metales pesados. En este contexto, el presente estudio evalúa las propiedades de adsorción de ocho muestras de celulosa no modificadas aisladas de la biodiversidad del Ecuador, como un potencial adsorbente de iones metálicos presentes en el agua. Las muestras aisladas se caracterizaron utilizando las técnicas de espectroscopia infrarroja por transformada de Fourier (FTIR), difracción de rayos X (XRD), microscopía electrónica de barrido (SEM), análisis termogravimétrico (TGA) y Brunauer-Emmett-Teller (BET) para comprender las propiedades fisicoquímicas. La prueba de adsorción de metales pesados utilizando 2 mM y 10 mM de solución de cobre demuestra que la celulosa no modificada puede adsorber iones de Cu^{2+} de manera efectiva, logrando una capacidad de reducción de $88,75 \pm 2,49\%$ y $54,96 \pm 2,5$, respectivamente. Además, los estudios de isotermas de adsorción revelan que F25 se ajusta mejor al modelo de Langmuir y OP al modelo de Freundlich. La máxima capacidad de adsorción fue 40 mg/g utilizando F25 y 60 mg/g usando OP. Estos resultados indican que el adsorbente a base de celulosa de una fuente natural puede ser una posible solución ecológica para el tratamiento del agua por contaminación de iones metálicos.

Palabras Clave: metales pesados, agua contaminada, celulosa natural, biodiversidad, adsorción.

Abstract

Heavy metals water contamination from various anthropogenic sources is a major concern in the globally community due to its negative impact on human and aquatic systems. Cellulose-based adsorbents have attracted attention as alternative materials due to their non-toxic and biodegradable characteristic. Among the water treatment methods, adsorption has gained interest due it is simplistic procedure, low-cost, and sustainable alternative technology for removing heavy metal traces. In this context, the present study evaluates the adsorption properties of the eight unmodified cellulose isolated from the ecuadorian biodiversity as a potential heavy metals ions decontaminant. The isolated samples were characterized using Fourier transform infrared spectroscopy (FTIR), X-ray diffraction (XRD), Scanning electron microscopy (SEM), thermogravimetric analysis (TGA), and Brunauer-Emmett-Teller (BET) methods to understand the physicochemical properties. Heavy metals adsorption test using 2mM, and 10mM of the copper solution, demonstrates that the unmodified cellulose can adsorb Cu^{2+} ions effectively, achieving $88,75 \pm 2,49\%$ and $54,96 \pm 2,51$, at respective concentrations. Additionally, adsorption isotherms studies reveal that F25 fits better to Langmuir and OP fit to Freundlich models, reaching the maximum adsorption capacity of 40 mg Cu per gram and 60 mg Cu per gram of adsorbate. These results indicate that the cellulose-based sorbent from a natural source can be a potential eco-friendly solution to water treatment from heavy metals ions.

Keywords: *heavy metals, polluted water, natural cellulose, biodiversity, adsorption*

Contents

List of Figures.....	xiii
List of tables	xvii
1. Introduction	1
2. Motivation	3
2.1. Problem Statement.....	3
2.2. Hypothesis and Objectives.....	3
2.2.1. Hypothesis	3
2.2.2. General objectives	4
2.2.3. Specific objectives.....	4
3. Theoretical Framework	5
3.1. Cellulose	5
3.2. Adsorption process.....	6
3.3. Cellulose-based adsorbent for remediation of polluted water	6
3.4. Common process in wastewater treatment	8
3.5. Current innovations to heavy metal removal from water	8
3.6. Adsorption Isotherms models	9
3.6.1. Langmuir Isotherms.....	9
3.6.2. Freundlich isotherm.....	10
3.7. Characterization Techniques.....	10
4. Experimental	13
4.1. Materials	13
4.1.1. Natural Source Raw Material	13
4.1.2. Reagents.....	13
4.2. Methodology	13
4.2.1. Cellulose Extraction Protocol.....	13
4.2.2. Standards Heavy Metal Solutions.....	14

4.2.3.	Batch Adsorption Studies	14
4.2.4.	Isotherm studies	15
4.2.5.	Statistical Analyses	16
4.2.6.	Samples Characterization	17
4.2.7.	Fourier transform infrared spectroscopy	17
4.2.8.	X-ray diffraction	17
4.2.9.	UV-Visible- Near Infrared Spectroscopy	18
4.2.10.	Scanning Electron Microscopy	18
4.2.11.	Energy Dispersive X-Ray Spectroscopy	18
4.2.12.	Thermogravimetry analysis	18
4.2.13.	Brunauer - Emmett-Teller	18
5.	Results and discussion	19
5.1.	Characterization of commercial cellulose	19
5.1.1.	Fourier transform infrared spectroscopy	19
5.1.2.	X-ray diffraction	20
5.1.3.	Scanning Electron Microscopy	20
5.1.4.	Thermogravimetry analysis	21
5.2.	Characterization of cellulose samples extracted from natural sources	22
5.2.1.	Fourier transform infrared spectroscopy	22
5.2.2.	X-ray diffraction	24
5.2.3.	Scanning Electron Microscopy	26
5.2.4.	Thermogravimetry analysis	28
5.3.	Batch adsorption studies	30
5.3.1.	Standards Heavy Metal Solutions	30
5.3.2.	Raw material - Heavy Metals Removal Percentage Studies	32
5.3.3.	Cellulose - Heavy Metals Removal Percentage Studies	33
5.4.	Brunauer- Emmett-Teller	36
5.5.	Elemental composition analysis	37
5.6.	Isotherms studies	41
5.6.1.	F25 Langmuir and Freundlich model fitting	41
5.6.2.	OP Langmuir and Freundlich fitting	44
5.7.	Statistical analysis	49
6.	Conclusion & Outlook	53

References 54
Annexes 59
 Annex A..... 59
 Annex B..... 63
 Annex C..... 67

List of Figures

Figure 1.	The chemical structure of cellulose is linked by (1–4) glycosidic bonds, adapted from Johnsy George et al. ¹⁹	5
Figure 2.	Adsorption mechanism adapted from Rahman et al ²⁵	6
Figure 3.	Characterization equipment (A) FTIR, (B) XRD, (C) UV-Vis-NIR, and (D) SEM.	11
Figure 4.	FTIR spectra for commercial microcrystal cellulose.	19
Figure 5.	X-ray graph for commercial microcrystal cellulose.	20
Figure 6.	SEM micrograph of the commercial microcrystal cellulose at (A) 300X and 1000X.	21
Figure 7.	Thermogravimetry profile analysis of commercial microcrystal cellulose.	21
Figure 8.	FTIR spectra comparison samples extracted from natural sources and commercial cellulose (CMC).....	22
Figure 9.	Comparative FTIR spectra of cellulose, hemicellulose from literature ⁴⁸ (A) and this work (B).	23
Figure 10.	X-ray diffraction patterns of the natural cellulose particles: (A) F17, (B) F20, (C) F25, (D) F27, (E) F28, (F) T1, (G) OP, (H) CP.	25
Figure 11.	SEM micrographs of (A) CMC, and extracted cellulose which was able to adsorb copper ions (B) F17, (C) F20, (D) F25, (E) OP, and (F) literature ⁶⁵	26
Figure 12.	SEM micrographs of extracted cellulose which was not able to adsorb copper ions (A) F27, (B) F28, (C) T1, and (D) CP.	27
Figure 13.	Thermogravimetry analysis profile and its derivate respectively (A, C) which presents and (B, D) and not present adsorption effect.....	29
Figure 14.	Uv-Vis-NIR absorption spectrum of Cu ²⁺ ions aqueous solution.	31
Figure 15.	(A) Calibration curve of copper solutions and (B) the residual graph (at max peak: 810 nm).	31
Figure 16.	Percent of reduction of Cu ²⁺ ions at high concentration (10mM), using the raw materials.	32
Figure 17.	SEM graph as raw material for (A) F25, and (B) OP.....	33
Figure 18.	Percent of reduction of copper ions (2mM) after treatment with control and natural cellulose using 5mg/ml.....	34
Figure 19.	Percent of reduction of copper ions (10mM) after treatment with control and natural cellulose using 5mg/ml.....	35

Figure 20. Percent of reduction of Cu^{2+} ions at low concentration (2mM), using three different mass (1mg/ml, 3mg/ml 5mg/ml).	35
Figure 21. Reduction percentage of Cu^{2+} ions at high concentration (10mM), using three different mass (1mg/ml, 3mg/ml 5mg/ml).	36
Figure 22. Distribution of the SSA correlated to the PV of the samples and the control	37
Figure 23. SEM image of F25 cellulose: (A) before and (B) after adsorption.	38
Figure 24. F25 elemental analysis after reaction with Cu^{2+} solutions (map resolution 32x20 pixel). 38	
Figure 25. F25 spectrum of elemental analysis.....	39
Figure 26. CMC elemental analysis after reaction, (A) SEM image with spots, and (B) spot 1 spectrum and elemental percentage.	40
Figure 27. F27 elemental analysis after reaction, (A) SEM image with spot, and (B) spectrum and elemental percentage.....	40
Figure 28. (A) Linear regression graph corresponds to Linearized-Langmuir function, and (B) table of covariance analysis values of F25.	41
Figure 29. (A) Cu^{2+} Langmuir isotherm adsorption Linearized and not Linearized of F25 (B) and their residual respectively.....	42
Figure 30. (A) Linear regression graph corresponds to Linearized-Freundlich function, and (B) of covariance analysis values of F25.....	43
Figure 31. (A) Cu^{2+} Freundlich isotherm adsorption linearized and non-linearized of F25 (B) and their residual, respectively.....	43
Figure 32. Experimental data fitted to Cu^{2+} ions adsorption isotherms models using F25 adsorbent. 44	
Figure 33. (A) Linear regression graph corresponds to Linearized-Langmuir model, and (B) table of covariance analysis values of OP.....	45
Figure 34. (A) Cu^{2+} Langmuir isotherm adsorption Linearized and not Linearized of OP, and (B) their residual respectively.....	45
Figure 35. (A) Linear regression graph corresponds to Linearized-Freundlich function, and (B) table of covariance analysis values correspond to OP.....	46
Figure 36. (A) Cu^{2+} Freundlich isotherm adsorption linearized and non-linearized of OP, and (B) their residual respectively.....	46
Figure 37. Experimental data fitted to Cu^{2+} ions adsorption isotherms models using OP adsorbent. 47	
Figure 38. Cu^{2+} ions adsorption isotherms models comparison between F25 and OP extracted from the natural source	49
Figure 39. (A) Residuald randon distrubion plot, (B) residual histogram, (C) regresion of experimental and predicted values and (D) statistic parameters values.	51
Figure 40. X-ray diffraction patterns graph comparison between samples extracted from natural sources and commercial cellulose (CMC).....	59

Figure 41. Uv-vis spectra after reaction C^{2+} ions (2mM) with the cellulose F25 and F25 using 3mg/ml	59
Figure 42. Uv-vis spectra after reaction C^{2+} ions (10mM) with the cellulose F25 and F25 using 3mg/ml	60
Figure 43. Percent of reduction of Cu^{2+} ions at low concentration (2mM), using the raw materials (without treatment).....	60
Figure 44. Fourier-transform infrared spectra of cellulose particles from natural sources: (A) F17, (B) F20, (C) F25, (D) F27, (E) F28, (F) T1, (G) OP, (H) CP.....	61
Figure 45. Thermogravimetry analysis profile of the (A) extracted cellulose, and the (B) peaks with the high weight loss.....	62
Figure 46. Photographs taken during the research project.....	67

List of Tables

Table 1. Adsorption capacities of some cellulose-based material. Adapted from Varghese et al. ²⁴ and Bethke et al. ¹¹	7
Table 2. Cu ²⁺ ions standard solutions for calibration curve.	14
Table 3. Cu ²⁺ ions initial solutions for isotherms experiments	16
Table 4. Factors and their respectively levels.	17
Table 5. Peaks assignments of the vibrational in the FTIR spectra	20
Table 6. Thermal degradation temperature of significant weight loss.	30
Table 7. Pore volume, sample surface area, and crystallinity index of samples.	36
Table 8. Isotherms parameters recovered from F25 and OP data.....	48
Table 9. Statistical values of the full factorial design.	50
Table 10. Some predicted values of OP and F25.....	52
Table 11. Data of adsorption test using 1mg/ml.....	63
Table 12. Data of adsorption test using 3 mg/ml.....	64
Table 13. Raw data of adsorption test using 5 mg/ml.	65
Table 14. Data of isotherms adsorption studies and fitting.	66

Chapter 1

Introduction

Heavy metals pollution is an unavoidable byproduct of anthropogenic activities, and many industries, causing severe environmental and health problems ¹. Heavy metals are elements having an atomic density greater than 5 g/cm^3 . The most frequent metal ions found in untreated water are cadmium (Cd), zinc (Zn), lead (Pb), mercury (Hg), arsenic (As), silver (Ag), chromium (Cr), iron (Fe), platinum (Pt), and copper (Cu) ¹⁻³. These ion concentrations have been found as the main contaminant in European soils and groundwater ⁴ and exceeding the maximum concentration limits (MCL) of Pb and Cr in Guayaquil drinking water⁵. Among the heavy metals, Cu^{2+} ions are considered a primary pollutant in water. These ions are not biodegradable and can bio-accumulate in living beings ⁶. Therefore, heavy metal ion removal from water is a great concern.

Copper is a naturally occurring metal that has an atomic number of 29 and a molecular weight of 63,546 *uma* ⁷. Cu is easily dissolved in the water and can be found in volcanic rock and groundwater. Nevertheless, the major contamination sources are humans, industries, and agricultural wastewater. Because of its excellent ductility and electrical and thermal conductivity, it is widely employed in the industry. Furthermore, Cu is also used as a nutritional supplement for animals and plants, which cause accumulation and eventually pollution of groundwater ⁸. According to the United States Environmental Protection Agency (US EPA), the MCL of the copper is 1,25 mg/L (20 μM) ⁹, while according to World Health Organization is 2 mg/L (WHO) for drinking water ¹⁰. Nonetheless, research has revealed that a high concentration of Cu in water causes imbalance cellular homeostasis, hemolysis, diarrhea, abdominal pain, vomiting, and several neurodegenerative diseases, for instance, Wilson, Alzheimer, and Menkes ^{6,11}. Thereby, detection and removal of copper ions trace present in water is needed.

Several methods to remove the heavy metals ions, including Cu, have been studied. These methods include chemical precipitation, flocculation, electrochemical treatment, membrane filtration, photocatalytic, and adsorption/bio-adsorption. Among them, the adsorption-based process is very attractive because it is a simple, cost-effective, and sustainable alternative for removing heavy metal traces ³. However, some of these methods have been limited by the cost, or it is not suitable for drinking water or not possible on a large scale. Materials with

high adsorption capacities, such as activated carbon, have been explored, but it is not universal for metal ions¹². Then, alternatives methods are still required. In this context, biodegradable material such as cellulose has attracted much attention to metal ions removal.

The accumulation of adsorbate on the adsorbent surface is referred to as chemical or physical adsorption. Cellulose-based materials have been studied in the field of water remediation via the sorption process. However, the adsorption capacity of cellulose is limited due to a lack of negative charges¹³. Additional functionalization is frequently conducted to address this constraint, yielding good results but complicating the process and increasing the cost¹⁴. Therefore, cellulose having adsorption capability without any additional chemical modification has greatly interested the scientific community and industry. In this context, some cellulose samples were isolated from various ecuadorian natural sources. Later, the materials were subjected to batch heavy metal (copper) experiments under established conditions. Copper was used as a model heavy metal to study the adsorption of cellulose since the Cu adsorption behaviors are similar to cadmium, palladium, lead, mercury, chromium, uranium, and nickel¹³. Furthermore, its availability in the laboratory and easy analysis with conventional equipment available in our laboratory. Finally, these were characterized using several techniques to confirm the binding process and statistically analyzed to show the significance of the adsorption capacity.

Chapter 2

Motivation

2.1. Problem Statement

Ecuadorian population is divided into 62% urban and 38% rural. Only 74 percent of rural residents have access to a type of water household installation, whereas 96 percent of urban residents do⁵. Inadequate access to safe drinking water, particularly in low and middle-income nations that include Ecuador, causes health issues. Water pollution from heavy metals is rising as a result of human activities such as mining and industry. Several environmental pollutions have been caused in Ecuador by artisanal and illegal mining. The heavy metals induce toxicity and cause damage to kidneys, liver, and genetic and neurological alterations. Some Ecuadorian rivers contain heavy metals derived from mining; for instance, a high Pb(II) concentration in Puyango river was found. However, this water is used in agriculture and for human consumption¹⁵. More research in Ecuador indicates that the concentration of several heavy metal ions in drinking water exceeds the World Health Organization guideline. For example, Guayaquil has a higher lead content in its drinking water. Cadmium and lead are present in the Estero Salado (Guayas province). Finally, the water treatment process in Ecuador uses the traditional procedures such as aeration, coagulation, flocculation, sedimentation, filtration, and disinfection using chlorine^{5,16}. In this way, developing an effective, low-cost alternative technology for removing contaminants from water is required to maintain the amount of drinking water balanced before it is irreparably damaged.

From this perspective, this work proposes using some ecuadorian plants to extract cellulose and use it in water remediation from heavy metals.

2.2. Hypothesis and Objectives

2.2.1. Hypothesis

Natural cellulose extracted from the ecuadorian biodiversity can exhibits heavy metal adsorption properties to use in water treatment.

2.2.2. General objectives

To test the heavy metal adsorption capacity of unmodified cellulose extracted from different plant sources.

2.2.3. Specific objectives

- To extract cellulose from eight different natural sources using an established protocol.
- To perform physicochemical characterization of extracted cellulose (i.e. F17, F20, F25, F27, F28, T1, OP, and CP) using FTIR, XRD, SEM, TGA, and BET.
- To test copper ions adsorption capacity of natural cellulose using commercial cellulose as control.
- To perform elemental characterization.
- To fit the data to Langmuir and Freundlich isotherms.

Chapter 3

Theoretical Framework

3.1. Cellulose

Cellulose is the most prevalent biopolymer found on the earth and forms the major biomass. This polymer can be found mainly in plants in their skeletal wall conformation organized in layers. Furthermore, cellulose also can be found in bacteria, fungi, algae, and even tunicates¹⁷. Wood pulp is the most common raw material source for cellulose^{18,19}. Cellulose is a polymer composed of hundreds to thousands of repeats of $\beta(1 \rightarrow 4)$ linked D-glucose units. Chemically is defined as a consistent monomer of $(C_6H_{10}O_5)_n$ (Figure 1). The length depends on the monomeric unit in the formula represented by n ; its number gives the degree of polymerization (DP). Cellulose presents good chemical, mechanical, rheological, and optical properties, and it is characterized by its hydrophilicity, chirality, biodegradability, and broad chemical modifying capacity²⁰.

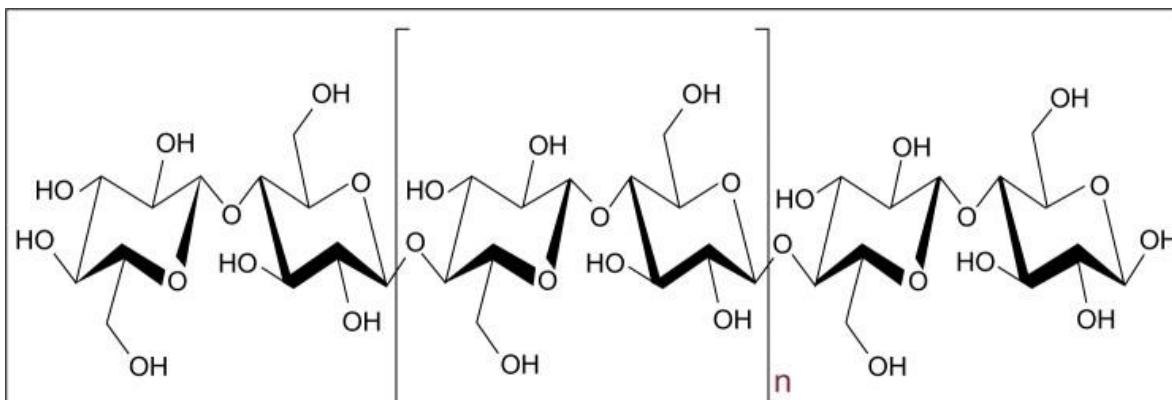


Figure 1. The chemical structure of cellulose is linked by (1–4) glycosidic bonds, adapted from Johnsy George et al.¹⁹.

The cellulose surface has abundant hydroxyl groups (-OH), which allow a functionalization enhancing the physicochemical properties. Moreover, -OH groups are responsible to form strong hydrogen bonds, giving them crystallinity and amorphous regions. The crystallinity region could define the long degradation process. Due to the large bioavailability, easy processing, non-toxic, biodegradable, and unique properties which depend on origin, it is

interesting to study and use in biomedical applications, optical detection, food packing, pharmaceutical, biofuel, and to water remediation, etc²¹⁻²⁴.

3.2. Adsorption process

Adsorption is the accumulation of the adsorbate contained in the solution on the adsorbent surface. The surface area is the main material property that is influent in this process because it gives more available active sites. The adsorption process first involves the transportation of the sorbent to the external surface. Later, it is transported within the pores of the adsorbent. Finally, some adsorbate is deposited on the surface, forming mono or multilayers (Figure 2)²⁵.

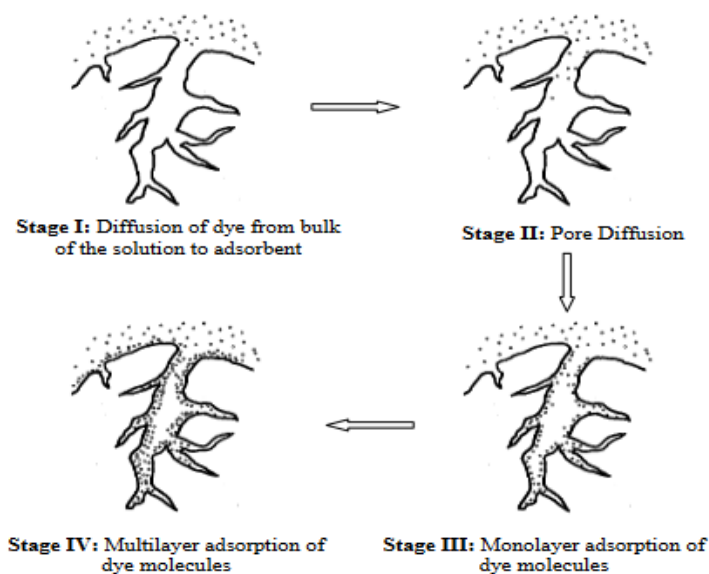


Figure 2. Adsorption mechanism adapted from Rahman et al²⁵.

3.3. Cellulose-based adsorbent for remediation of polluted water

Water treatment and safety are concerning global problems. Indeed, it needs to find alternatives way to purify. Cellulose is the most abundant polymer, and environmental sustainability is of great interest at small and large-scale to remove water pollutants. In water purification, this polymer could be applied on large filters to remove heavy metal traces from the water after the conventional treatment or a small filter for drinking water on individual levels.

In recent years, numerous efforts have been made to prove the adsorption capacity of the cellulose-based material particularly, to remove heavy metals ions at low concentrations¹³.

Natural fibers such as coir pitch, rice husk, banana peel, oil palm fiber, sugarcane bagasse, and beetroot have been used to remove water pollutants (as heavy metals) due that there are abundant, low cost, eco-friendly, and available in large quantities. Natural fibers are composed of cellulose, hemicellulose, lignin, extractives, and inorganics. Many studies focused on cellulose due to its unique properties, such as its hydrophilic, processability, insoluble in many solvents, crystalline, and no-toxic behavior²⁵. Researchers found that pristine cellulose has a low adsorption capacity to heavy metals, as a reference in the range of 0,11 – 0,2 mmol/g of Cu²⁺¹³. Nevertheless, functionalization can drastically improve the removal performance. The functionalized approach includes grafted, alkaline treatment, esterification, halogenation, and oxidation methods. Table 1 summarizes studies on copper ion removal using cellulose-based adsorbents without any modification and with modifications. The research found interesting behaviors of polyethylenimine (PEI) cross-linked paper since it shows the high adsorption capacities of copper ions^{11,22,24}. Moreover, this can work for anionic and cationic ions because after modification, some amine groups were neutral while some were cationic, the neutral bind to metal cations, and the cationic bind to anions²⁵.

Table 1. Adsorption capacities of some cellulose-based material. Adapted from Varghese et al.²⁶ and Bethke et al.¹³.

Cellulose-based adsorbent	Modification (binding functional group)	Adsorption capacity
Orange peel	---	63 (mg/g)
Oil palm shell	---	1,75 (mg/g)
Rice Husk	---	30.0 (mg/g)
Pomegranate peel	---	30,12 (mg/g)
Cellulose bead	Sodium hydroxide (carboxyl)	70,5 (mg/g)
Cellulose powder	Acrylic acid (carboxyl)	17,2 (mg/g)
Wood pulp	Citric acid (carboxyl)	24 (mg/g)
Cellulose	Succinic anhydride (carboxyl)	0,47 mmol/g
Cellulose	Acrylic acid (carboxyl)	5,17 mmol/g
Cellulose	Methyl benzalaniline	157,3 mg/g
Sawdust	Alkaline treatment	0,040 mmol/g
Cellulose nanofibrils	Mechanical disintegration	0,2 mmol/g
Wood pulp cellulose	Citric acid (carboxyl)	0,37 mmol/g
Cellulose	Linked 8-hydroxy-quinolone	0,63 mmol/g
Cellulose	TEMPO oxidation, PEI grafting (carboxyl and amine)	0,82 mmol/g
Cellulose	Triethylenetetramine (amine)	0,94 mmol/g
Kapok fiber	Diethylenetriamine pentaacetic acid (DTPA)	1,6 mmol/g
Wood pulp	Glycidyl methacrylate and imidazole	1,75 mmol/g
Cellulose sugarcane bagasse	1,3-Diisopropyl-carbodiimide (amine)	1,79 mmol/g
Cellulose Paper	PEI-crosslinked	6,84 mmol/g

The adsorption capacity difference of the oil palm shell could be explained by the particle size and the purpose of the work, the study used in the range of 6.5-8 mm due to objective to use in constructed wetland wastewater treatment system. Larger particle size adsorbs less amount of ions due to the reduce surface area, more tortuous and longer diffusion pathway to the internal surface and it is explained by the greater diffusional resistance in larger particle²⁸. In another study using oil palm shell found a capacity of adsorption around 28 mg/g, however they used particle size less than 75 μm ²⁹. In the case of rice husk authors used a size particle size less than 1 mm and also they attribute to the content of lignin and silica which have been recognized to facilitate the adsorption process³⁰.

3.4. Common process in wastewater treatment

The wastewater passes through three or four stages. Each stage is involved methods to remove pollutants. Primary methods involve the sedimentation of the solid presence in the wastewater. For this purpose, the fluid is passed through the tanks where sludge content is retained. The secondary methods use the oxidation process to further wastewater purification. This process can be done by bio-filtration, aeration, and oxidation ponds. Bio-filtration uses sand, contact, or trickling filter to ensure additional sedimentations. Aeration uses microorganisms such as microbes converting the matter into energy, carbon dioxide gasses, and water. It is a long but effective process. A tertiary method is used to remove the impurities, such as small organic compounds, including traces of heavy metals ions, to convert them into good quality water and even drinking water. Methods include chemical precipitation, electrochemical oxidation, reverse osmosis, ion exchange, membrane technologies, and adsorption to remove heavy metals ions³¹. Nevertheless, these methods are limited by the cost, incomplete removal, selectivity to the pH, fouling, high-energy consumption, and not are greener technologies^{32,33}.

3.5. Current innovations to heavy metal removal from water

An important point in water remediation is that the materials used are not pollutants after use. Nanotechnologies have shown a great potential to manufacture and improve the efficiency of the materials. The literature described metallic and metal oxide (MNMs), carbon-based and organic nanomaterials. MNMs include silver, titanium oxide, and iron base nanoparticles had been used to remove heavy metals from water. These exhibit fast kinetic and high adsorption capacities. Nevertheless, MNMs are challenging due to their toxicity, and it forms aggregations affecting the reactivity. Carbon-based nanomaterials, including activated carbon, carbon nanotubes, and graphene, have been employed for photocatalytic remediation, increasing the cost. Carbon-based materials in their pristine form are inert, thus demanding a surface modification, but it is a complex process burdening in industrial applications. The

organic nanomaterials include mainly chitin, chitosan, and cellulose; however, the chitin and chitosan come from animals. In this way, cellulose nanomaterials (CNMs) have become a great interest in the research as emerging alternative technologies because biodegradable materials do not generate waste ^{3,12}.

CNMs include nanocellulose, nanocrystalline cellulose, cellulose nanowhiskers, and cellulose nanofibers have unique physical properties at the nanoscale. These materials can be isolated from different methods and sources. The methods include acidic treatment, TEMO oxidation, and enzymatic reaction ¹⁷. CNMs are promising due to the high surface-area-to-volume ratio, low cost, and easy functionalization, increasing the binding sites in the adsorption process. Furthermore, CNMs have interesting properties such as being environmentally friendly, self-assembly, reinforcing capabilities, and high mechanical strength ³⁴. CNMs also have been studied as the main component of membrane filtration. It gives high tensile strength to support the water pressure. Furthermore, CNMs can be blended to form electrospun nanofibers with a large diameter of the fibers resulting in membrane mats with small pores size ¹⁴. Nanofibers for water treatment are currently widely studied.

Another innovation for water mediation includes composites and microbial fuel cells (MFC). Composites are interesting due to the possibility of combining two or more materials to enhance performance. This material could require less time to reach the maximum adsorption capacities. Among these materials, the cellulose-based hydrogel has been studied to remove copper ions obtaining a maximum capacity of 1.4 mm/g ³⁵. Microbial fuel cells have been demonstrated to be a promising technology because they use the organic matter present in the water to produce electricity. It is used with metal ions with higher redox potential, including copper, mercury, and silver. A study demonstrated the removal efficiency using a low concentration of 20 mg/L ³⁶. Then, they present MFC as an alternative method to remove heavy metal ions and simultaneously bioenergy recovery. Nevertheless, their challenges are in the inability to treat all metals ions, pH depending, and the deterioration or removal efficiencies ³⁷.

Among the innovative technologies, the adsorption process to remove heavy metal ions using cellulose materials has proven to be an efficient, simple, green, clean and low-cost method for wastewater treatment using biodegradable and non-toxic materials as cellulose ²⁶.

3.6. Adsorption Isotherms models

3.6.1. Langmuir Isotherms

Langmuir isotherm is used to describe a complete monolayer formation of the sorbent onto the surface. It assumes that the sites are equally active and distributed uniformly across the

surface and are limited by the number of available places³⁸. There is no interaction between the adsorbent molecules. In addition, this model assumes homogeneous adsorption energy upon the surface and no interactions between the adsorbed ions³⁹. It is defined in equation 1⁴⁰.

$$q_e = \frac{q_m K_L C_e}{1 + K_L C_e} \quad (1)$$

Where q_e represent the metal ions adsorbed at equilibrium (mg/g), q_m is the maximum adsorption capacity of the material (mg/g) which express a complete monolayer formation C_e is the concentration of metal ions remaining in the solution (mg/L), and K_L is the empirical Langmuir constant (L/mg).

3.6.2. Freundlich isotherm

Freundlich isotherm is not restricted to the monolayer formation and includes heterogeneous surfaces with interactions between the adsorbent molecules assuming multilayer adsorption. This model analyses the relationship between non-ideal and reversible adsorption process with engagement between molecules adsorbed⁴¹. This model is defined in the equation 2⁴⁰.

$$q_e = K_F C_e^{\frac{1}{n_F}} \quad (2)$$

Where, q_e (mg/g) is the adsorption capacity at equilibrium, C_e is the concentration of the metal ion remaining in the solution (mg/L), K_F the empirical Freundlich constants associated with the capacity, and $1/n_F$ is the empirical Freundlich constants associated with adsorption intensity. According to the n_F values is possible to obtain some characteristics: if $2 < n < 10$, means good adsorption, if $1 < n < 2$, means poor adsorption, and if $n < 1$, reveals difficult adsorption.

3.7. Characterization Techniques

The characterization techniques used in this work include: Fourier transform infrared spectroscopy (FTIR), X-ray diffraction (XRD), UV-Visible- Near-Infrared Spectroscopy (UV-Vis-NIR), Scanning Electron Microscopy (SEM), Energy Dispersive X-Ray Spectroscopy (EDS), Thermogravimetry analysis (TGA), Brunauer-Emmett-Teller (BET) (Figure 3).

The infrared region consists of three regions, near-infrared ($12800-4000\text{cm}^{-1}$), mid-infrared ($4000-400\text{cm}^{-1}$) and far-infrared ($400-10\text{cm}^{-1}$). FTIR is one of the most

common techniques used to identify different functional groups constituting a compound. It indicates the presence or absence of the functional groups. It is a rapid and not destructive technique for the quantitative and qualitative determination of the biomass compound. The resulting spectrum comes from the molecular vibration mechanism, which refers to energy-matter interaction^{42,43}. Despite the advantages, FTIR characterization is still challenged due to the overlapping bands. In particular, in the fingerprint region, because of several peaks⁴⁴.

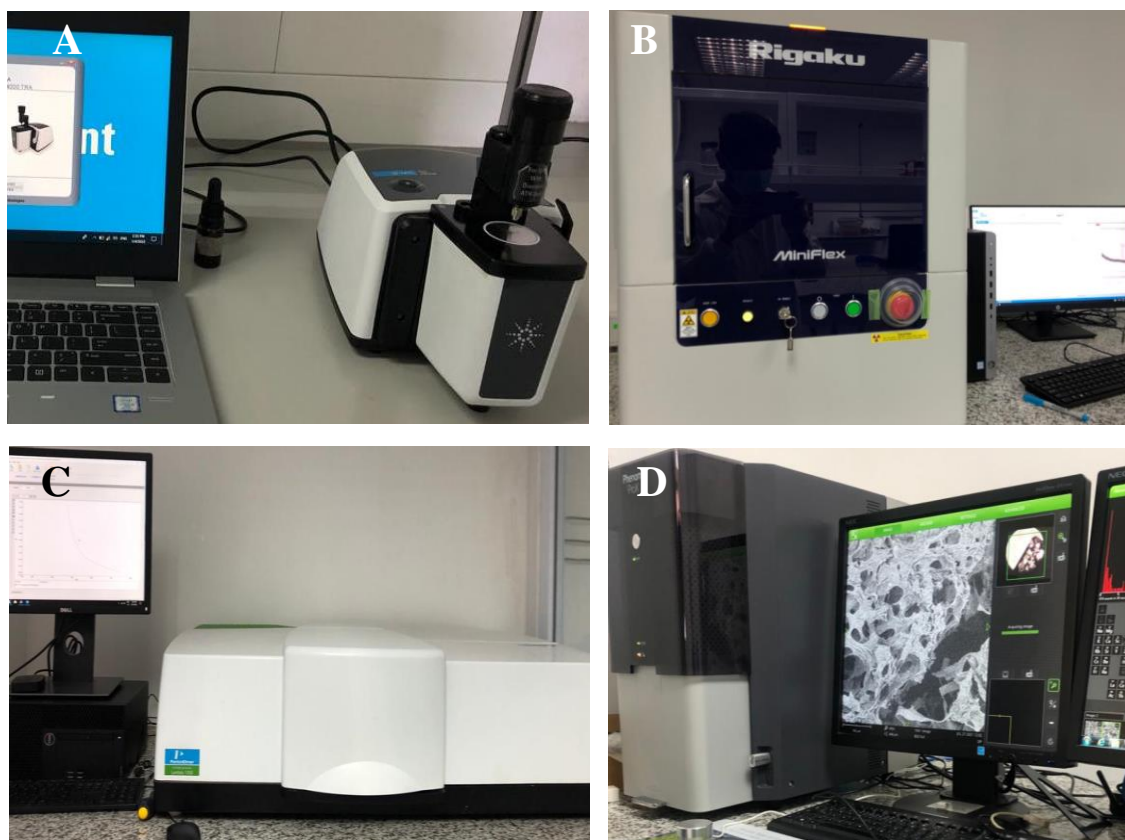


Figure 3. Characterization equipment (A) FTIR, (B) XRD, (C) UV-Vis-NIR, and (D) SEM.

The existence of crystalline in cellulose is one of the most critical factors influencing its physical, chemical, and mechanical properties. XRD gathers information on the atomic arrangement within the unit cell that repeats infinitely along with all three Cartesian coordinate directions. Diffraction occurs the incident beams collide with a periodic array of molecules in unit cells. The incident beams are generated by an x-ray source with wavelengths around 0.1 nm . The positions of the diffracted beams are governed by the positions of the atoms in the unit cell of the crystal, and it satisfies Bragg's law for constructive interference, $n\lambda = 2d \times \sin\theta$ ⁴⁵.

SEM is a powerful tool to examine the morphology of the material at micro and nano-scale. Images are produced from the reflected electrons after the interaction of the electron beam with the specimen surface. At the output, the sample surface topography with a high spatial resolution is obtained since the electron waves are 10^5 times shorter than the visible light. The main component of SEM equipment is the electron source that accelerates electrons with energy levels in the range of 0,1 – 30 keV, electromagnetic lenses to control the shape and trajectory of the electron beam, and a high vacuum environment that allows moving the electrons without scattered or absorbed by the air⁴⁶. TGA is a tool used to investigate thermal stability, polymer filler content, moisture content, and material composition. TGA measures weight changes in materials as a function of temperature or time in a controlled environment. It is accomplished by raising the temperature and releasing volatile materials. The output plot illustrates the weight of the sample vs. temperature, indicating the thermal transition until total material disintegration⁴⁷.

EDS, also known as EDX, is an analytic method for the chemical characterization of the sample. It can be used in combination with SEM to obtain a near-surface elements component and their amount. The amount can be expressed as weight or atomic percentage. Regularly, elements in concentrations of at least 1% are detected. The analysis is performed by spot or mapping a determinate area map. The output is a colorful image representing each element with one color and a spectrum plotted as x-ray counts vs. energy⁴⁸. The BET analysis method effectively determines the surface area of a particular substance. It aims to explain the physical adsorption of gas molecules. This effect is induced by Van der Waals forces generated by an adsorbate film. Nitrogen gas is an adsorbent in BET analysis because it does not react with the material surface. Specific surface area is proportional to the quantity adsorbed and is calculated using BET theory, which assumes multilayer adsorption of the gas on the adsorbent surface⁴⁹.

Chapter 4

Experimental

4.1. Materials

4.1.1. Natural Source Raw Material

The natural material studied in this work comes from eight different Ecuadorian sources; the codification of the samples is: F17, F20, F25, F27, F28, T1, OP, and CP. The F17 raw material was collected from the Botanic Garden of Yachay Tech located at San Miguel of Urcuquí. F27, T1 and OP was purchased on fruit section at Mercado Urcuquí (San Miguel of Urcuquí, Imbabura, Ecuador). The raw material corresponding to F20, F25, F28, and CP were purchased at Mercado Amazonas, located in Ibarra City (Ibarra, Imbabura, Ecuador).

4.1.2. Reagents

Copper (II) sulfate pentahydrate was used to prepare heavy metal solutions. The commercial cellulose microcrystal (CMC) was used as a control. Both reagents were supplied by Sigma-Aldrich (St Louis, MO 63103, USA).

4.2. Methodology

4.2.1. Cellulose Extraction Protocol

Laboratory equipment and chemical reagents were used for the cellulose extraction process, including a beaker, analytic balance, centrifuge, falcon tubes, spatula and acid, base, solvents, and bleach reagents to treat the raw material to obtain just the cellulose part. It follows an established protocol consisting of grinding the samples, acid/base treatment, bleaching, and multiple washing to samples purification from the chemicals residuals (more details about the protocol and sources are restricted for this thesis). All samples were processed using the same protocol to prevent changes in the properties of cellulose due to changes in the extraction protocol.

4.2.2. Standards Heavy Metal Solutions

In order to get the calibration curve, different amount of the $\text{Cu}_2\text{SO}_4\cdot\text{H}_2\text{O}$ was weighted. The metal precursor was diluted in distilled water to obtain a concentration in the range (Table 2). Later, the solutions were measured using a Uv-Vis-NIR spectrophotometer to analyze the wavelength that corresponds to the maximum peak.

Table 2. Cu^{2+} ions standard solutions for calibration curve.

Cu^{2+} [mM]	Cu^{2+} [mg/L]
1,01	64,40
2,08	132,19
5,68	360,95
10,23	650,22
15,01	953,61
20,86	1325,26
30,22	1920,32
40,54	2576,08

Table 2 shows the initial standard concentration used to set the calibration curve expressed in mM and ppm.

4.2.3. Batch Adsorption Studies

The cellulose extracted from natural sources (F17, F20, F25, F27, F28, T1, OP, CP) and commercial cellulose was used for all batch experiments to absorb heavy metal ions. A certain amount of cellulose was weighted (1mg/ml, 3mg/ml, and 5 mg/ml) as appropriate for the test and added to the falcon tube (15 ml). After that, 10 ml of initial concentration set at 2mM or 10mM of Cu^{2+} was added and stored for the reaction. The mixture was centrifuged and separated into the solid and liquid parts. The liquid part, which contained the residual concentration of metal ions, was measured using a UV-Vis-NIR spectrophotometer at λ_{max} 810 nm to determine the residual concentration. All experiments were repeated three times. Finally, the solid part was stored to further characterization.

The heavy metal ions removal percentage (RP) for the given conditions was calculated using the following equation ⁵⁰.

$$RP = \left(1 - \frac{C_f}{C_o}\right) * 100 \quad (3)$$

Where the C_f represent the final solution concentration (mM or mg/L) at a certain time, and C_o express the initial concentration of the metal ions solution used for the experiments.

4.2.4. Isotherm studies

Isotherms studies were done similarly to the batch adsorption studies. It was done only for the material that shows potential adsorption capacities (OP and F25). The amount of cellulose was 3mg/ml, and initial Cu^{2+} concentrations were set between 2mM and 30mM. (130 mg/L – 1900 mg/L) at pH of 5 in environmental conditions (Table 3). The solutions were stored for 24 hours to reach the equilibrium time.

The obtained experimental data were fitted to the classic Langmuir and Freundlich models defined in the theoretical section. For this purpose, it was based on the linearized forms according to equations 4 and 5, respectively ⁵¹. Moreover, the non-linear analysis was computed using Microsoft excel SOLVER and compared to the data of the linear isotherm. The highest correlation coefficient, SSE, and variance analysis indicated which model fitter better.

$$\frac{1}{q_e} = \frac{1}{q_m K_L C_e} + \frac{1}{q_m} \quad (4)$$

$$\log q_e = \frac{1}{n_F} \log C_e + \log K_F \quad (5)$$

To verify the linear adjustment of the linear model of Langmuir and Freundlich, the variance analyses were performed, obtaining statistical values corresponding to typical error, lower and upper limits, probability, F critical, and R^2 for both; the intercept and the slope of the regression line. In addition, for Langmuir model the equilibrium parameter was calculated according to equation 6. It is an adimensional constant and is important for this model ⁴¹.

$$R_L = \frac{1}{1 + K_L * C_0} \quad (6)$$

K_L (L/mg) is Langmuir constant and the C_0 is the initial concentration (mg/L). R_L indicated the nature and the shape of the adsorption, when $R_L > 1$, the adsorption is not favorable, when $R_L = 1$ is linear, when the $0 < R_L < 1$, the adsorption is favorable, and when $R_L = 0$, the adsorption is reversible.

The heavy metal ions uptake quantity for the material was calculated using the following equation ³⁹.

$$Q = \frac{(C_0 - C_t) V}{m} \quad (7)$$

In the equation 7, Q express the material adsorption capacity (mg/g) of metal ion, C_0 (mg/L) is the initial concentration of the Cu^{2+} solutions, C_t is the Cu^{2+} concentration at certain time.

$V(L)$ represents the volume used for the reaction, and $m(g)$ is the weight of the dry adsorbent material.

Table 3. Cu^{2+} ions initial solutions for isotherms experiments

Cu^{2+} [mM]	Cu^{2+} [mg/L]
2,08	132,19
4,02	255,48
6,01	382,00
10,23	650,22
11,99	761,80
15,01	953,61
20,86	1325,26
25,06	1592,56
30,22	1920,32

4.2.5. Statistical Analyses

The results of this work were statistically analyzed using a full factorial design (FFD) with three factors according to the general equation 8. The full factorial design studied the impact of all variables and their interactions on the outcome. Typically, the levels are labeled as high and low, or 1 and 0.

$$y = \mu + A + B + C + AB + AC + BC + ABC \quad (8)$$

In this equation, μ (%) represents the means of the reduction percentage, A expresses the cellulose source (CMC, F17, F20, F25, F27, F28, T1, OP, CP), B is the amount of cellulose mass (1mg/ml, 3mg/ml, and 5mg/ml), C represent the heavy metals concentration (2mM and 10mM) and AB, AC and BC is the second-order interactions, and ABC is the third-order interactions. The second order of interaction is: $A*B$ means interaction between the source and the amount of cellulose, and $A*C$ represents the interaction between the cellulose source and the concentration. At the same time, $B*C$ implies the interaction between the amount of cellulose and the heavy metal concentrations. In addition, the $A*B*C$ expresses an interaction between all factors.

The levels for concentration were high (1) and low (0), while for the amount there were -1, 0, and 1 to corresponding amount 1mg/ml, 3mg/ml, and 5mg/ml respectively. Data is summarized in table 4.

Table 4. Factors and their respectively levels.

Source	Concentration Levels	Mass Levels
F17, F20,		-1
F25, T1,	0	0
OP, CP, CMC	1	1

4.2.6. Samples Characterization

Extracted cellulose from natural sources and CMC were characterized using several techniques: FTIR, XRD, SEM, TGA, and BET. Furthermore, the pellet (cellulose after reacting with heavy metal solutions) was characterized by EDS to confirm copper binding.

4.2.7. Fourier transform infrared spectroscopy

FTIR was used to analyze the functional groups present in the samples. The FTIR spectra were obtained from the freeze-dried samples, and placed directly in the Cary 630 FTIR Agilent spectrometer equipped probe. The spectra were recorded in the range of 400 to 4000 cm^{-1} in absorbance mode with a resolution of 4 cm^{-1} after 8 continuous scans with a threshold of 0,002.

4.2.8. X-ray diffraction

XRD was used to determine the extracted cellulose nature and crystallinity using Miniflex-600, Rigaku powder diffractometer (Tokyo, Japan), with a D/tex Ultra2 detector with $\text{CuK}(\alpha)$ radiation source at 40 kV and 15 mA. Additionally, data was collected employing a $\theta/2\theta$ in the scan-axis with a $0,05^\circ$ step width in a scan range of $5-90^\circ$ in 2θ and the D/tex Ultra2 detector in 1D scan mode.

The Crystallinity Index (CrI) was calculated by the intensities of the crystalline ($I_{(002)}$) and amorphous ($I_{(am)}$) regions shown in the patterns according to the empirical method for estimating the degree of CrI of native cellulose proposed by Segal et al ⁵². using the following equation.

$$CrI = \frac{I_{(002)} - I_{(am)}}{I_{(002)}} * 100 \quad (9)$$

From the equation 9, CrI expresses the relative degree of crystallinity, I_{002} represents the crystalline of the sample at the maximum peak intensity (in arbitrary units) 2θ angle close to 22° of the 002 lattice diffraction, and the I_{am} is the counter reading representing the amorphous region at the peak intensity 2θ angle close to 18° .

4.2.9. UV-Visible- Near Infrared Spectroscopy

Uv-Vis spectroscopy allows quantifying the concentration of the solution using the value of the absorbance. The absorption spectra were measured in the range of 350 to 900 nm using a LAMBDA 1050 UV-Vis-NIR spectrophotometer (Perkin Elmer, USA) with quartz cuvettes. After analyzing the spectra and finding the maximum peak of adsorption, the following measurements in the adsorption test experiments were recorded at a fixed wavelength. To measure, 2 ml of the liquid part from the adsorption experiments were used

4.2.10. Scanning Electron Microscopy

The surface morphology and microstructure of the extracted natural cellulose were evaluated by SEM microscopy. A small particle was placed on the carbon-coated grid and cleaned using compressed air. The samples were then assessed using a Phenom Pro X with a voltage excitation of 10 kV on a scale between 200 μm and 80 μm and a sample detector BSD Full.

4.2.11. Energy Dispersive X-Ray Spectroscopy

EDX technique was used to identify the elemental composition of sample material of the near-surface. First, the sample was dried down prior to analysis. Then, the characteristic energy for each atom was measured using a Phenom Pro X with a voltage excitation of 10 kV with an x-ray detector.

4.2.12. Thermogravimetry analysis

Cellulose samples (F17, F20, F25, F27, F28, T1, OP, CP, and CMC) were subjected to TGA analysis to study the range of weight loss due to the nature. For this purpose, lyophilized samples were placed in a thermogravimetry analyzer from 25°C to 950°C

4.2.13. Brunauer - Emmett-Teller

To determine the Sample Surface Area (SSA) and the Pore Volume (PV) per gram of the material, BET multipoint and BJH desorption method was used, respectively. A small amount of the sample was placed in a degassed Quanta chrome instrument, at heat temperature of 100°C with $10^\circ\text{C}/\text{min}$ and hold for 1440 minutes in N_2 flow.

Chapter 5

Results and Discussion

5.1. Characterization of commercial cellulose

5.1.1. Fourier transform infrared spectroscopy

Cellulose FTIR spectra are well known and studied. Figure 4 reflects FTIR spectra obtained from CMC, with cellulose characteristic peaks; $\sim 1000\text{ cm}^{-1}$ corresponds to C-C, C-OH, C-H ring, and side group vibrational band, a peak $\sim 1105\text{ cm}^{-1}$ representing a C-O-C glycosidic ether band. A great peak is evident at $\sim 3300\text{ cm}^{-1}$, $\sim 2900\text{ cm}^{-1}$, $\sim 1638\text{ cm}^{-1}$, and $\sim 1313\text{ cm}^{-1}$, corresponding to OH stretching vibration mode, $\text{sp}^3\text{ C-H}$ stretching, OH bending of absorbed water molecule present in cellulose, and CH_2 rocking vibrations at carbon six respectively. These peaks are in concordance found in the literature^{53,54}. Also, there are peaks corresponding to β -glycosidic linkage of cellulose, C-O-C stretching ring at $\sim 895\text{ cm}^{-1}$, and at 1053 cm^{-1} , respectively. Additionally, more peaks in the fingerprint region are summarized in table 5^{55,56}.

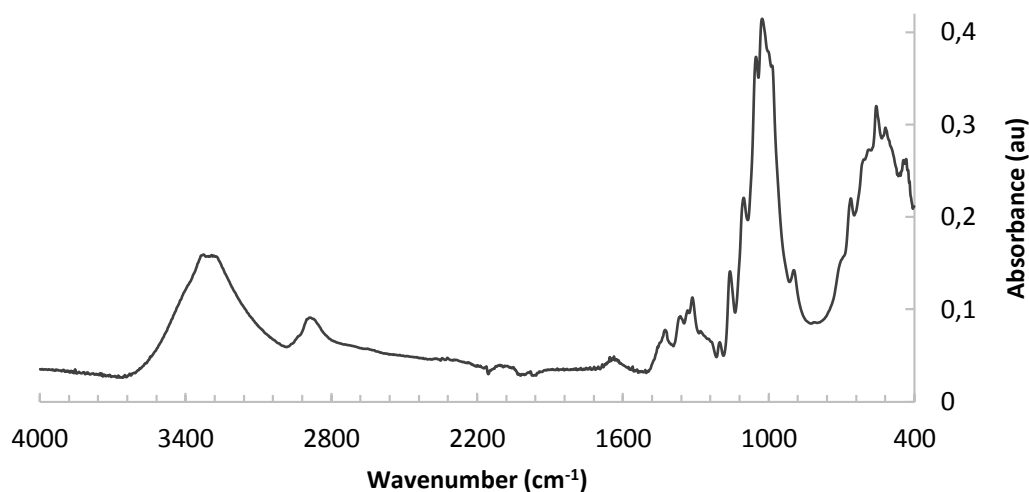


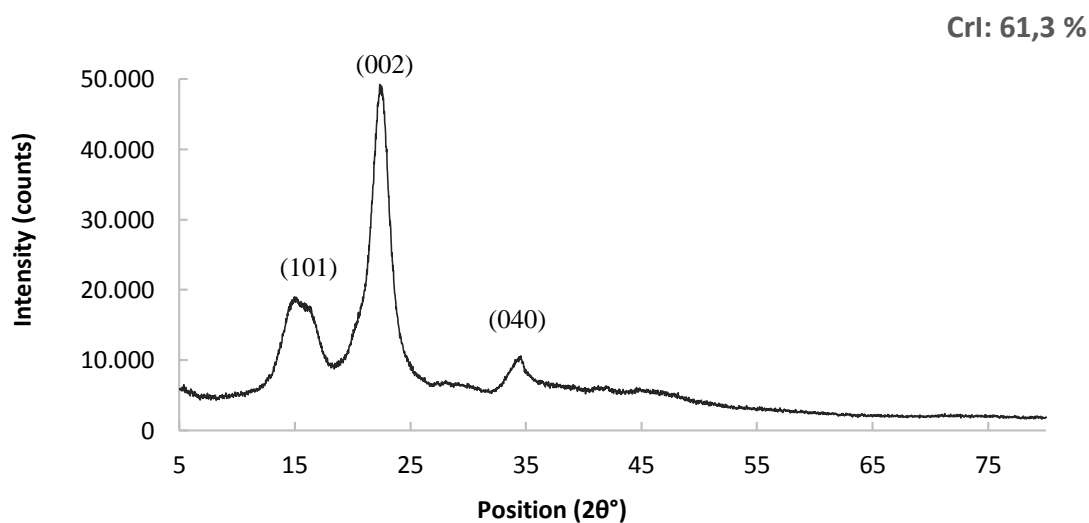
Figure 4. FTIR spectra for commercial microcrystal cellulose.

Table 5. Peaks assignments of the vibrational in the FTIR spectra

Wavenumber (cm ⁻¹)	Assignments
661	OH, out-of the plane bending
895	C-O-C stretching at β -glycosidic linkage
1053	C-O-C stretching ring
1165	Anti-symmetrical bridge C-O-C stretching
1200	C-O stretching
1334	C-O or CH in-plane vibration
1364	C-H bending
1425	C-H ₂ scissoring

5.1.2. X-ray diffraction

XRD analyzed the CMC crystallinity. Figure 5 illustrates the spectra and the CrI (61,3 %), similar to the literature^{53,57}. Moreover, it is clear to distinguish two prominent peaks close to 22° and 18° representing the crystalline and amorphous counterparts.

**Figure 5.** X-ray graph for commercial microcrystal cellulose.

5.1.3. Scanning Electron Microscopy

Figure 6 illustrates the SEM observations of commercial cellulose at low and high magnification showing a tube and rod-like structure, a compact and slight irregular surface. It has a uniform structure and size (20-40 μm).

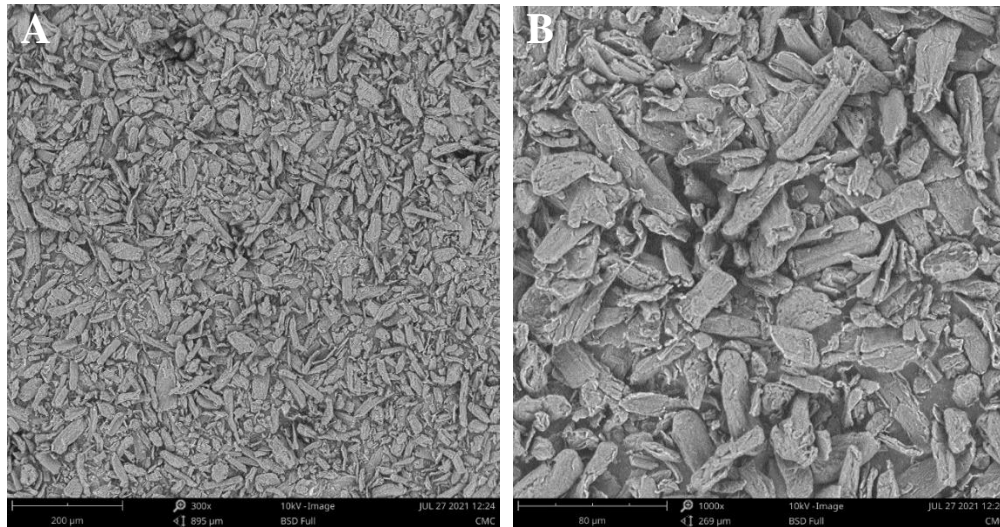


Figure 6. SEM micrograph of the commercial microcrystal cellulose at (A) 300X and 1000X.

5.1.4. Thermogravimetry analysis

The control TGA profile highlights a uniform weight loss because of the material purity, revealing a typical spectrum (Figure 7). CMC has a 6% weight loss until 100 °C, this could be attributed to the water evaporation, and the maximum weight loss rate occurs at 340 °C, corresponding to 86 %. It is associated with the expected cellulose thermal degradation ⁵¹.

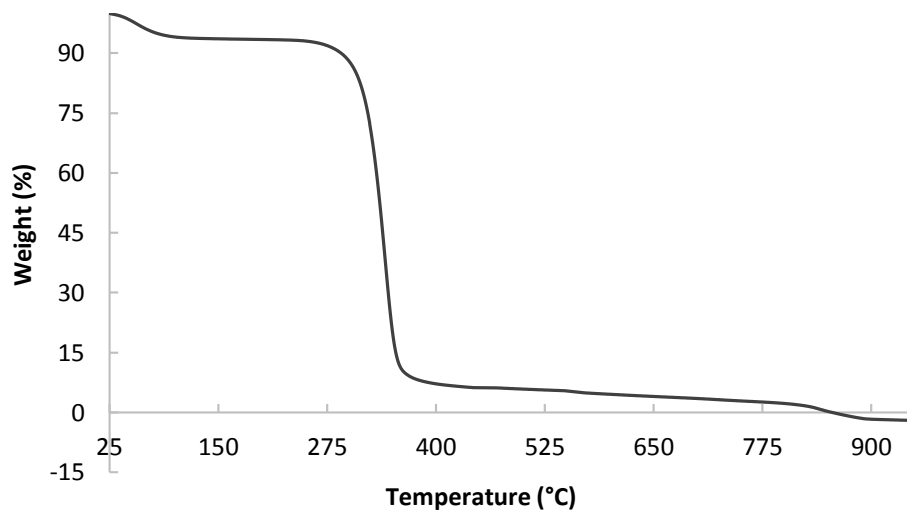


Figure 7. Thermogravimetry profile analysis of commercial microcrystal cellulose.

5.2. Characterization of cellulose samples extracted from natural sources

Several techniques were used to characterize cellulose structural, morphological, and chemical properties derived from various natural sources.

5.2.1. Fourier transform infrared spectroscopy

A typical cellulose FTIR spectra could be divided into two regions. The first region between 1500 cm^{-1} and 900 cm^{-1} is called cellulose fingerprint. The second region is called the functional group around 1500 cm^{-1} and 4000 cm^{-1} ^{58,59}. All extracted cellulose from natural sources indicates the characteristic peak of commercial cellulose. It means the purification treatment was effective. Figure 8 shows a broad peak between 3000 and 3700, and it is due to the OH-stretching coming from hydrogen in cellulose ⁵⁵. All essential peaks were identified according to our previous studies ^{53,54,57}.

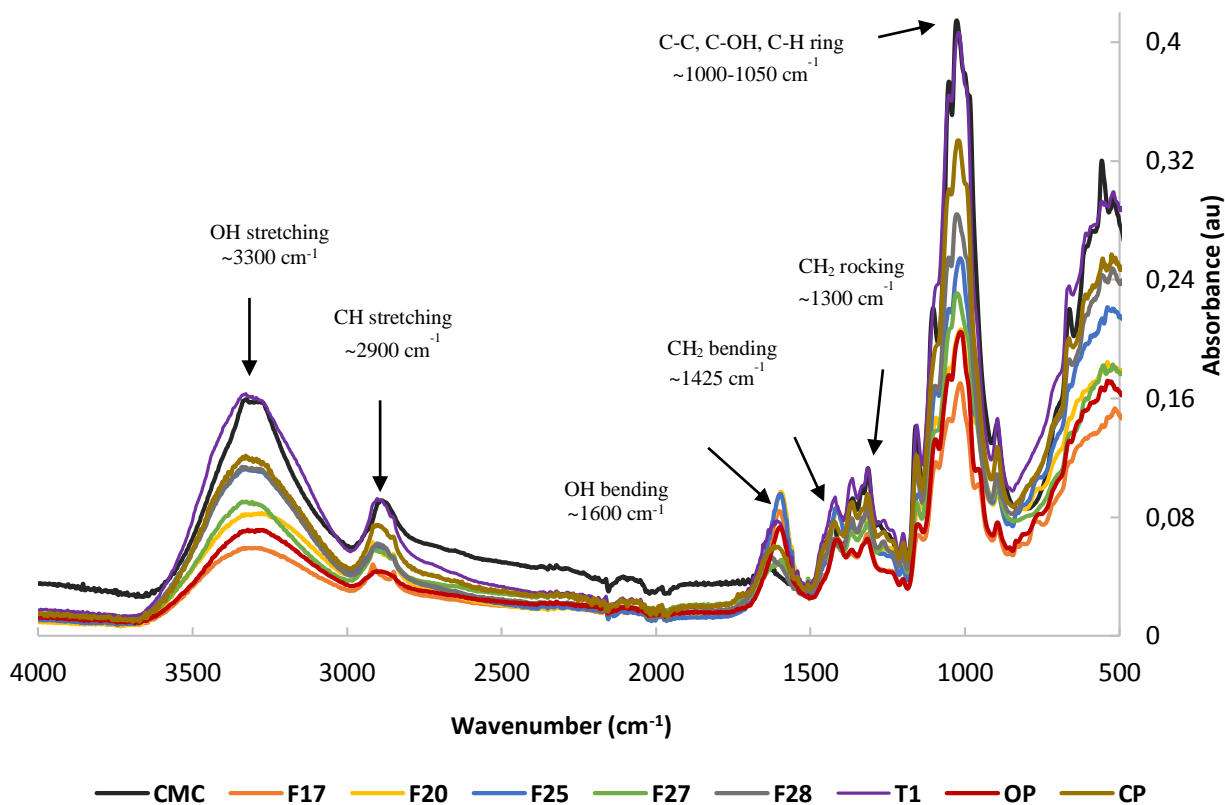


Figure 8. FTIR spectra comparison samples extracted from natural sources and commercial cellulose (CMC).

Nevertheless, there is a slight difference between the samples. F17, and F20 have additional peaks at 1735 cm^{-1} attributed to C=O stretching, 1245 cm^{-1} corresponding to CO of the glucuronic acid. These groups could be linked to small quantities of hemicellulose^{60,61}. F27, F28, T1, and CP share the peaks 1265 cm^{-1} which could represent C-O linkage in aromatic groups⁵⁶. Since the natural fibers are composed of cellulose and hemicellulose, lignin and extractives²⁵ the purity of the sample depends on the treatment used. Literature reports that the cellulose content in bamboo is 40-55% and 70-75% in flax¹³. According to the FTIR analysis, the presence of different peaks ($1735, 1265, 1245\text{ cm}^{-1}$) from the control could be attributed to a small quantity of hemicellulose or lignin in the sample.

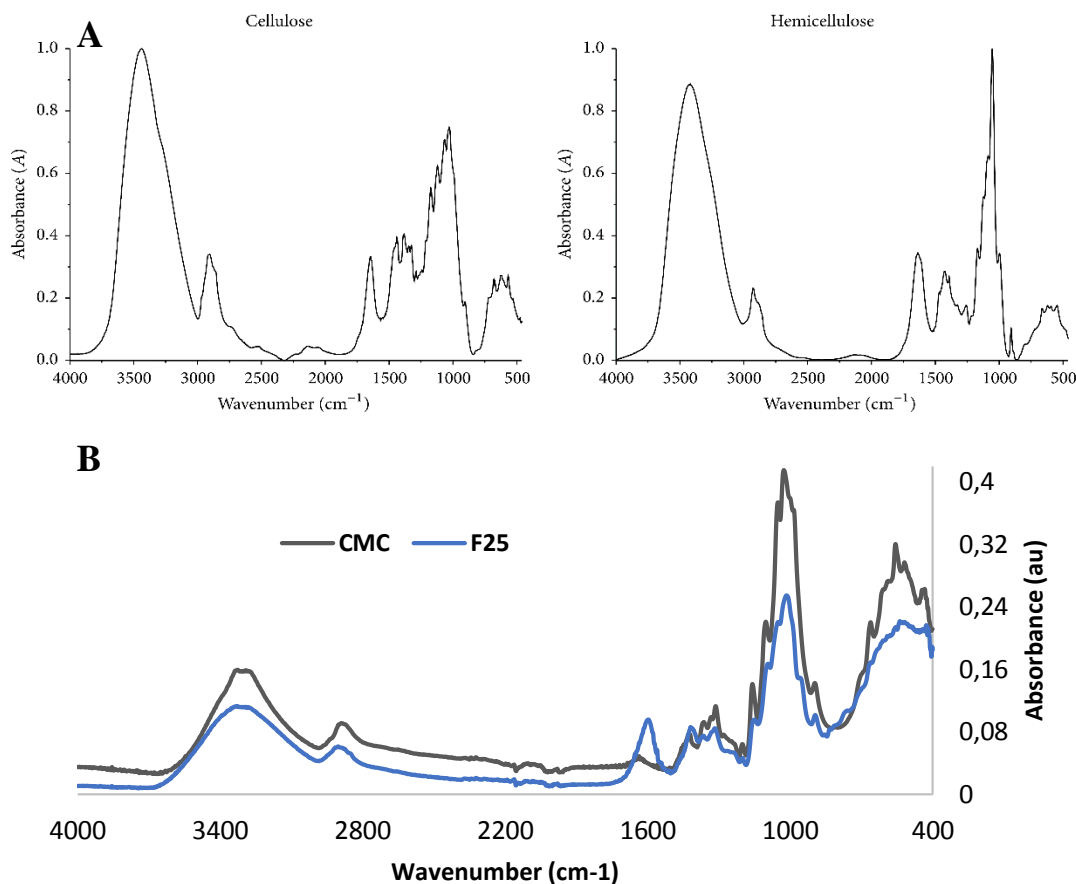


Figure 9. Comparative FTIR spectra of cellulose, hemicellulose from literature⁴⁸ (A) and this work (B).

On the one hand, the peaks at $1420\text{-}1430\text{ cm}^{-1}$ are associated with the amount of crystalline structure of the cellulose; then, there can be seen more intensity in F20 and F25 samples. This wavenumber corresponds to the symmetric CH_2 bending vibration⁴⁴, which is in concordance with the found crystalline index. On the other hand, the peak at 896 cm^{-1} corresponding C-O-C stretching at β -glycosidic linkage is associated with the amorphous region in cellulose^{43,44}. It agrees with the XRD-spectra found in OP and F17, which has a

low index concerning others. Figure 9 further compares the cellulose and hemicellulose from the literature and this study.

Figure 9 illustrates pure cellulose and hemicellulose FTIR spectra and the FTIR of this work. According to the previous figure, it was able to speculate the presence of hemicellulose, further supporting the idea since the profile of the commercial cellulose is observed to be identical to the commercial one. However, in the profile of the extracted sample, a difference in the peak can be observed close to a marked about 1600 cm^{-1} . The intensity of this peak exceeds the fingerprint at $1100\text{ -}1500$, and it can be observed in the hemicellulose spectrum. However, this comparison tells us that the extracted samples may have a hemicellulose content

5.2.2. X-ray diffraction

The mechanical and thermal properties of a material are determined by its crystalline and amorphous structure. The reinforcing capacity and mechanical strength of cellulose, in particular, are decisive factors in its usage in environmental remediation methods⁶². The crystallinity of the eight samples was examined by the XRD technique. The X-ray diffractograms are shown in Figure 10. The samples show major peaks at $2\theta=22,7$ and $2\theta=21,7$, corresponding to cellulose type I and II crystalline structure, respectively. The second peak, around $2\theta=18$ and $2\theta=16$, is associated with the amorphous cellulose types I and II.^{45,63} These diffraction peaks correspond to the crystallographic planes (002) and (110). Furthermore, a low-intensity peak is present at $2\theta=35^\circ$, corresponding to the plane (040)⁶⁴.

Since all diffractograms patterns of extracted samples show similarity in the peak position in I_{002} and I_{am} corresponding to $21,7^\circ$ and $15\text{-}16^\circ$, respectively, they are mainly compound by cellulose type II. It is in concordance with the literature that effective treatment can convert a native lignocellulose material to cellulose type II⁶³.

Nevertheless, the samples differ in the crystallinity index: F17 and OP show a low *CrI* ($\sim 30\%$), and F20 exhibits a high *CrI* degree ($50,3\%$). A structure with low crystalline can help in the adsorption process due to the internal organization of the chain, and the adsorption process mainly occurs in the amorphous regions. This occurs because, there is poor interaction between the biosorbent and the metal ions in the crystalline region. It is due to the low accessibility to the hydroxyl group because there they are more compact⁶⁰. That is why interactions (physical, chemical, ion exchange, electrostatic, aggregation)³ mainly occurs in the amorphous region since it shows more available active sites. Therefore, it agrees with F17 and OP, which show a good adsorption capacity but not F25, which also has a significant adsorption capacity. In addition, different *CrI* is related to the materials nature since all samples were treated with the same protocol.

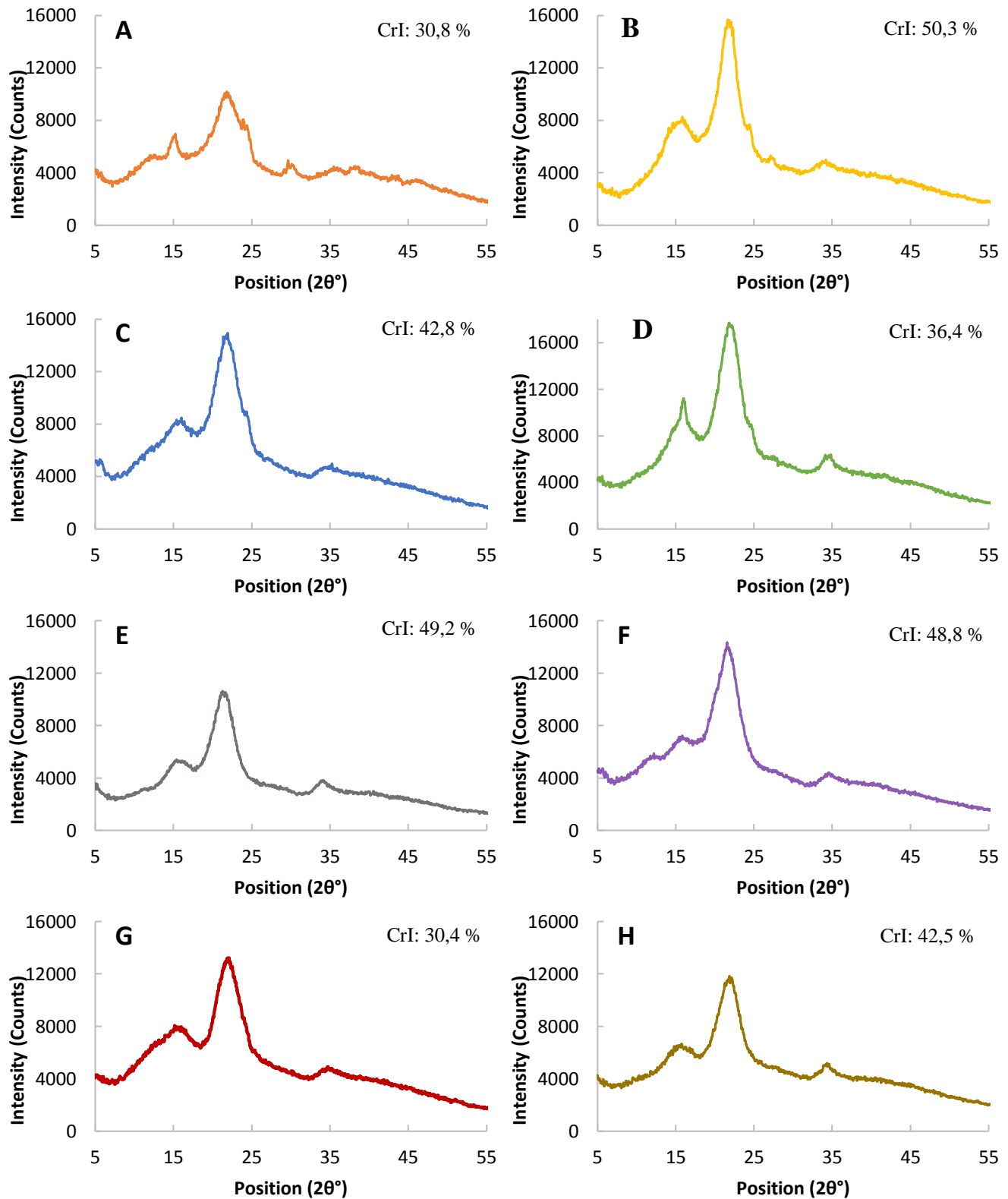


Figure 10. X-ray diffraction patterns of the natural cellulose particles: (A) F17, (B) F20, (C) F25, (D) F27, (E) F28, (F) T1, (G) OP, (H) CP.

5.2.3. Scanning Electron Microscopy

SEM analysis was performed to further investigate the eight extracted samples surface morphology. The subsequent figures (Figure 11, Figure 12) divide them into two groups. One group presents good adsorption properties, and another does not show adsorption properties.

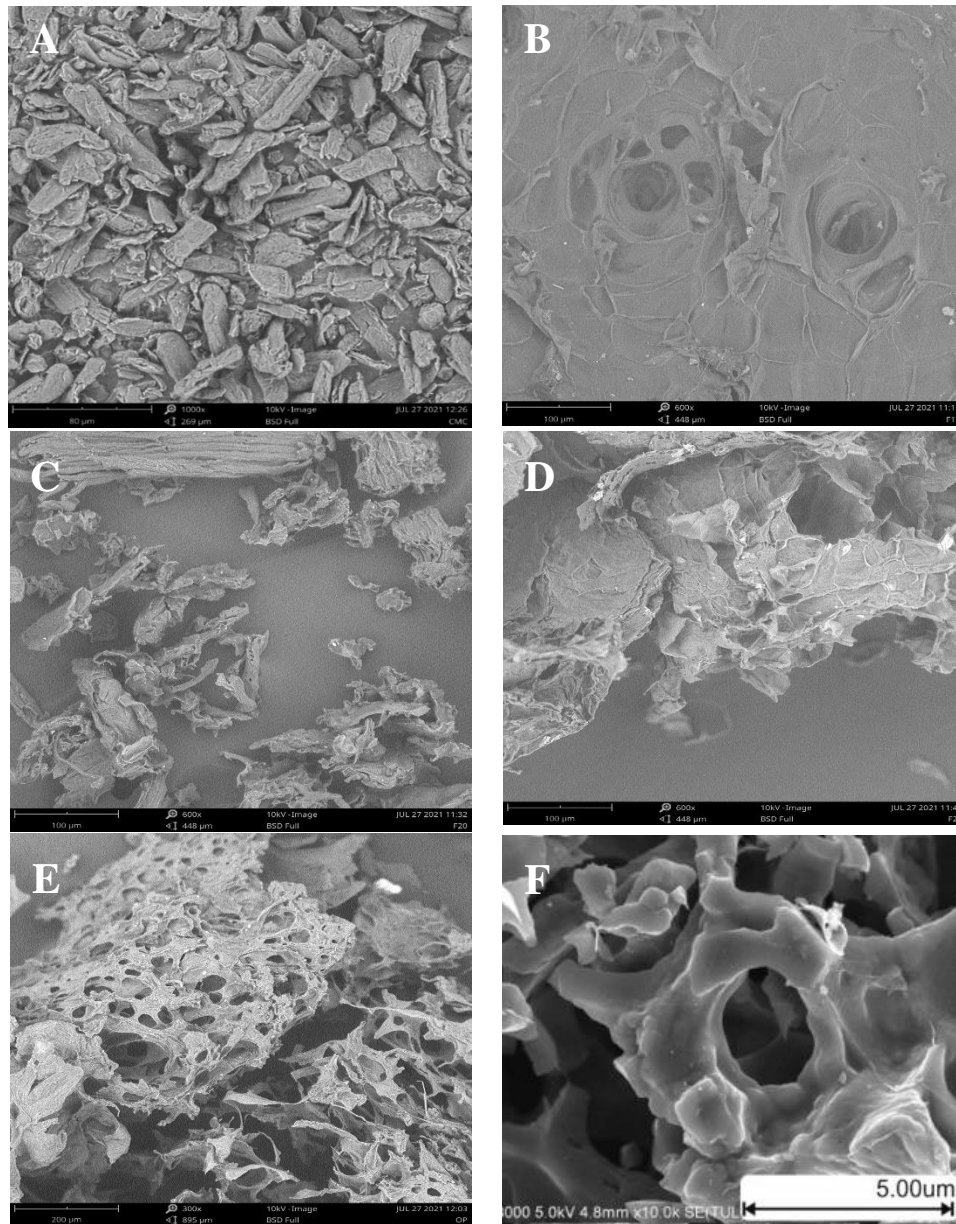


Figure 11. SEM micrographs of (A) CMC, and extracted cellulose which was able to adsorb copper ions (B) F17, (C) F20, (D) F25, (E) OP, and (F) literature ⁶⁵.

On the one hand, figure 11 shows SEM images of the samples, which show adsorption capacities, especially F17, F25, and OP. This figure also includes control SEM images and images found in literature from similar sources and treatments. F25 SEM graph depicts a porous morphology, giving them a high surface area to interact with sorbate and surface with irregularities and too roughness, which allow the adsorption process. Although F17 has no high porous structure, it has pretty amorphous. OP clearly shows similar morphology to the found in the literature. The amorphous regions are in concordance between the SEM graph and XRD profile for F17 and OP, which relate the irregularities and porosity surface structure with *CrI*.

On the one hand, the SEM graph in F27 and T1 (Figure 12) shows high irregularities and rough surfaces. F27 and F28 show uneven, pleated, and shriveled structures. On the other hand, CP offers a compact with slight irregularities at the fiber surface. F28 is a compact mass without porosities on the surface.

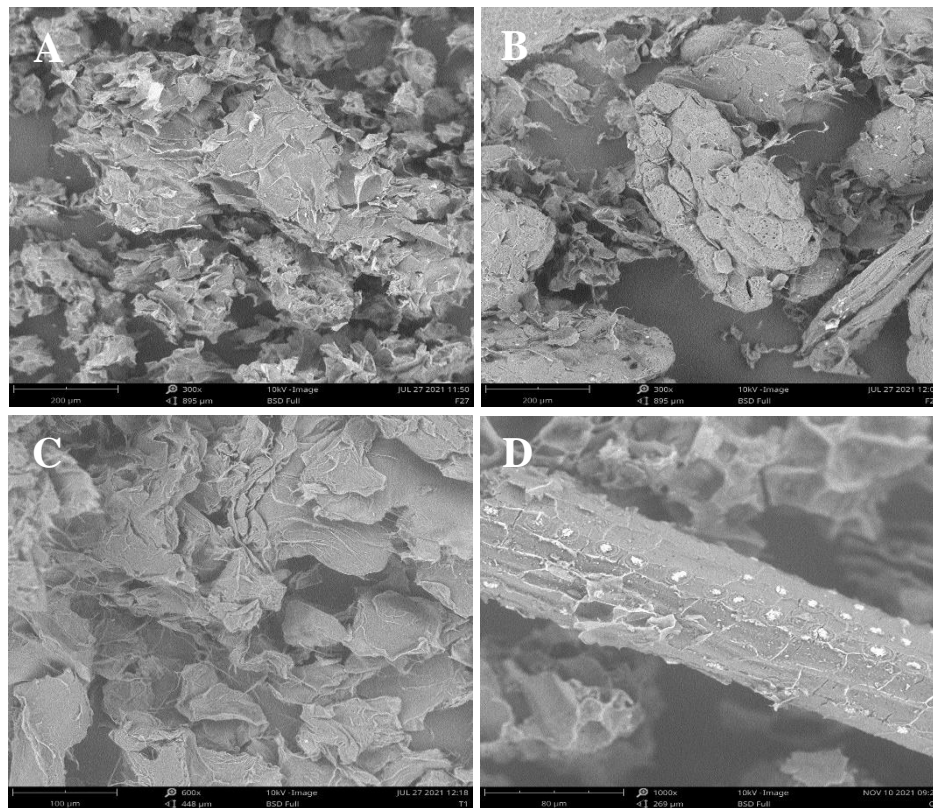


Figure 12. SEM micrographs of extracted cellulose which was not able to adsorb copper ions (A) F27, (B) F28, (C) T1, and (D) CP.

The SEM images present a unique structure of each sample, appearing as uneven pores, smooth, shriveled, and rugged, giving them highly irregular surfaces. Therefore, they can present a unique adsorption property and process that need contrast with another

physical/chemical characterization. The isolate differences could be associated to the material sources despite the fact the same treatment was used on each sample.

One of the main differences between the sample that show adsorption capacity and those that do not is the presence of porous and surface irregularities form. Although F27, F28, T1, and CP show uneven, pleated, and shriveled surfaces, these irregularities are very smooth. Moreover, the particle size is large. Instead, F25, F20, and OP present porous, and the surface morphology is too rough. Furthermore, the particle size is smaller. For example, the F20 SEM image shows size particles in 50 to 500 μm . According to the SEM image, the OP pore size ranges from 50 μm to 100 μm . Additionally, OP microstructure is different from others since they illustrate layer-by-layer formation with porous structure. This could help a vital role in the sorption process since they can allow a multilayer formation of the ions

5.2.4. Thermogravimetry analysis

Thermogravimetry analysis results show different thermal degradation profiles for each sample with certain similitudes. Therefore, the analysis was performed in two ways: A) general for all spectra divided into four regions, and B) separated into two groups that present adsorption capacities and do not present bio-adsorption properties for better understanding. The results are shown in figure 13.

All samples spectrum could be divided into three-stage of weight loss. The first stage occurs between 25-100 $^{\circ}\text{C}$ revealing a weight loss in the range of 6-13 %, which may be ascribed to the moisture traces released ⁶⁶. Another evident weight loss was found at 200-270 $^{\circ}\text{C}$, which could probably mean the presence of hemicellulose degradation because it has a random amorphous structure that promotes easy hydrolyzed. The samples that present a significant degradation in this region are F17, F20, F25, and OP, between 11% and 26 %. The third stage indicates a major weight loss occurred in the range of 270-400 $^{\circ}\text{C}$ between 20-65%. It is related to cellulose degradation since it is composed of a long polymer of glucose units with crystalline parts, enhancing thermal stability ⁴⁷. All samples have a significant loss in this stage. An interesting peak is found for OP in the second stage, with the same weight loss in the first and second stages. F17 and OP are in concordance with *CrI*, meaning the amorphous regions drive more easy degradation. Finally, after 400 $^{\circ}\text{C}$, the TGA profile indicates that there is still a noticeable weight change. This may be explained by the presence of lignin. Lignin decomposes a maximum rate observed at 350–450 $^{\circ}\text{C}$, according to the literature^{67,68}. Additionally, this has been confirmed in the characterization studies of *Ceiba aesculifolia* fibers, where lignin decomposition was observed above 377 $^{\circ}\text{C}$ ⁶⁹.

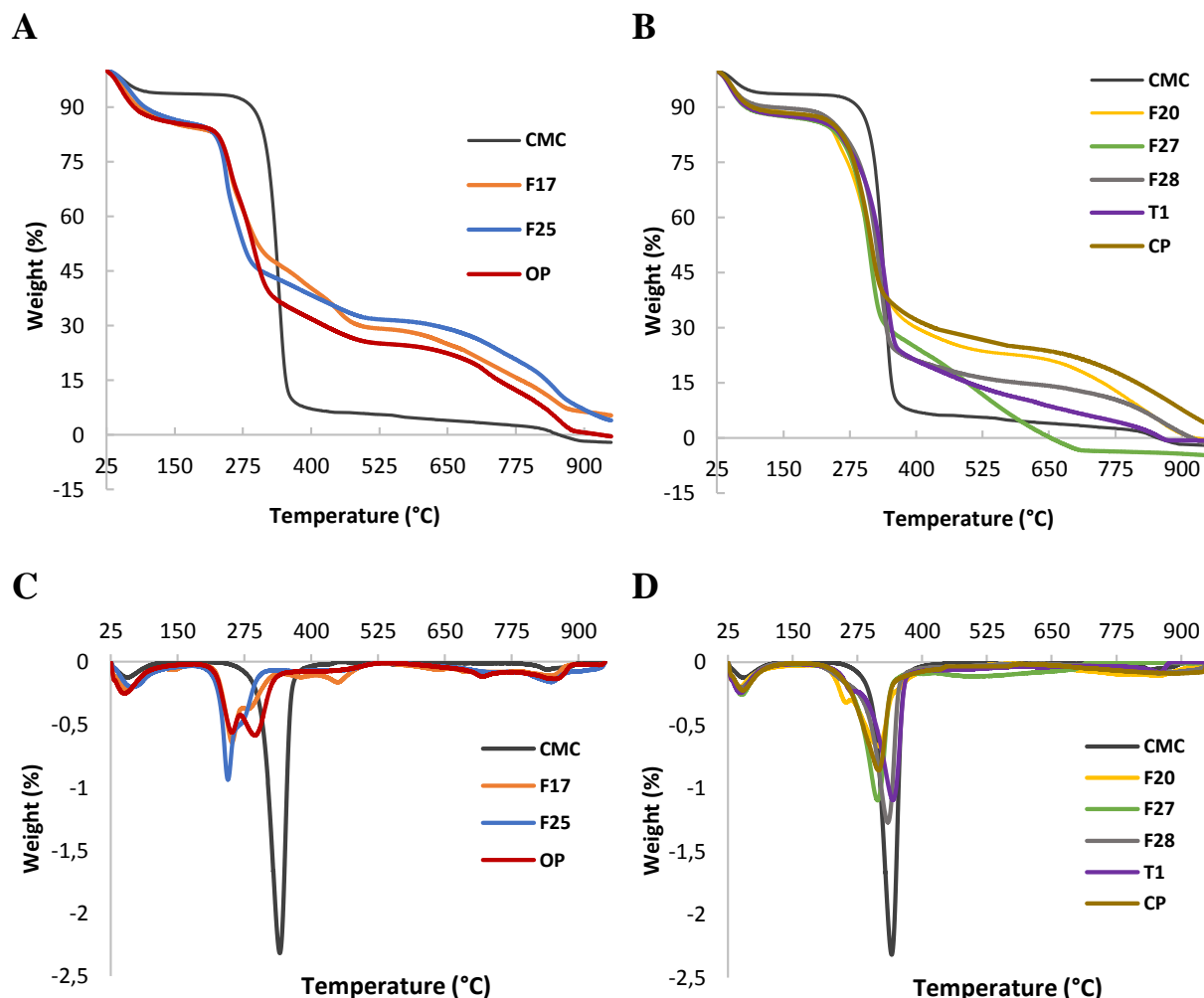


Figure 13. Thermogravimetry analysis profile and its derivate respectively (A, C) which presents and (B, D) and not present adsorption effect.

Figures 13A, 12C represents a samples profile with adsorption properties. They show a rapid thermal weight loss rate of around 250 °C. In addition, the TGA profile has a left shift, and the total mass loss occurs close to over the 950 °C. There is an important mass reduction in the range of 400-600 °C, which could be explained because of the volatile matter related to lignin⁷⁰. In contrast, in Figures 13B, 12C, all samples have a maximum weight loss rate in the third stage, and the total mass loss starts from 650 °C.

Table 6 summarizes the significant thermal degradation temperature and the interval with the maximum weight loss rate with the respective percentage.

Table 6. Thermal degradation temperature of significant weight loss.

Source	Temperature Interval (°C)	Maximal weight loss rate Temperature (°C)	Estimate percentage (%)	Total weight loss (°C)
CMC	B	340	86	855
F17	A	251	20	950+
	B	280	23	
F20	A	253	11	926
	B	315	45	
F25	A	245	25	950+
	B	360	20	
F27	B	312	60	653
F28	B	334	65	919
T1	B	343	55	861
OP	A	250	26	930
	B	293	30	
CP	B	315	55	950+

*A=(200-270)°C *B=(270-400) °C

The water content and the extractives can initiate the degradation process at low relativity temperatures and accelerate the degradation process reducing the thermal stability. A lower crystallinity can reduce the thermal stability in the degradation process. In this way, the thermal decomposition is shifted to a higher temperature when the *CrI* increases, highlighting a direct relationship between the thermal stability and crystallinity of the samples, which act as a barrier for heat transfer ⁴⁷.

5.3. Batch adsorption studies

5.3.1. Standards Heavy Metal Solutions

To understand if there are heavy metal adsorption properties on some of the eight extracted samples, a bath study using two different concentrations and three different adsorbent dosages was performed according to the methods section.

Figure 14 shows the characteristic Uv-Vis-NIR spectrum for Cu^{2+} obtained from the copper sulfate aqueous solutions. Later, the spectrum was analyzed using its derivate, and the wavelength corresponding to the maximum peaks was found at 810 nm. In addition, the spectrum clearly shows that when the concentration increases, the absorbance intensity increase.

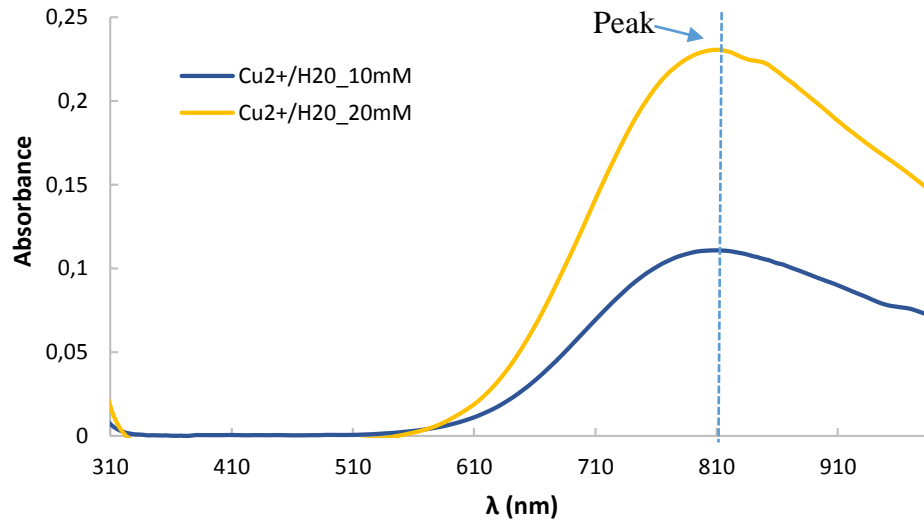


Figure 14. Uv-Vis-NIR absorption spectrum of Cu²⁺ions aqueous solution.

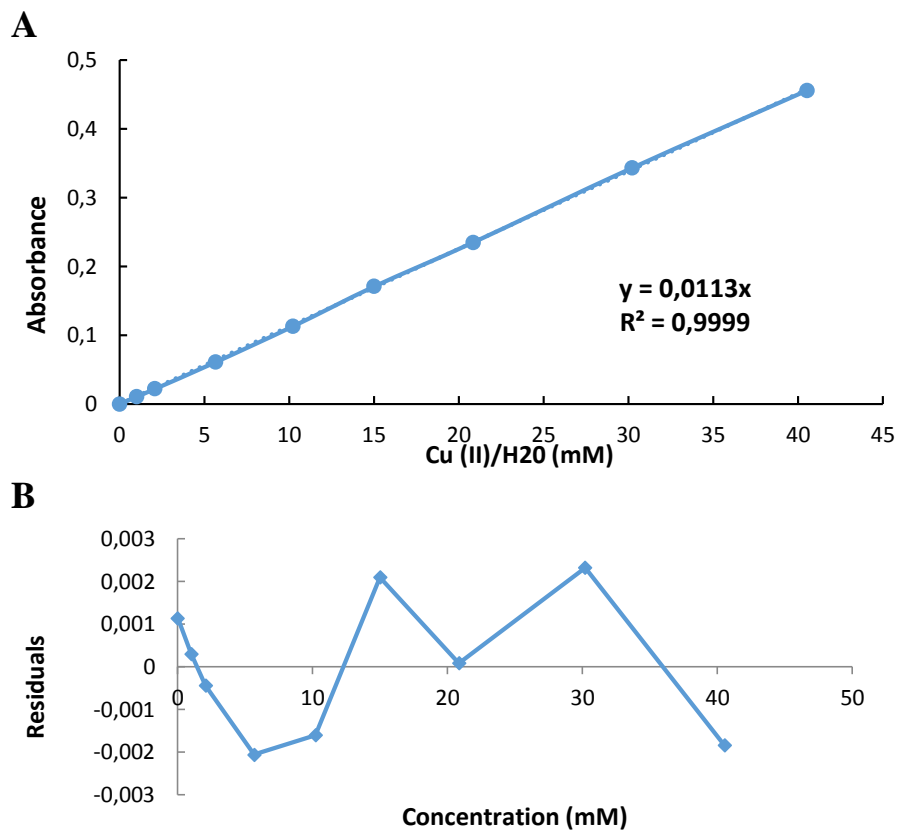


Figure 15. (A) Calibration curve of copper solutions and (B) the residual graph (at max peak: 810 nm).

As mentioned in the methods section, the remaining concentration was calculated using a calibration curve. Figure 15, illustrated the calibration curve and the residual plot. The result shows a strong linear correlation between the initial concentration and the absorbance values, which is demonstrated by the correlation coefficient $R^2 = 0,9999$. Moreover, the residual plot shows a random distribution confirming the previous statement.

The method limit of detection (LD) using the described spectrophotometer was calculated as three times the standard deviation of the blank. The computed value was $0,1184 \text{ mM}$. The concentration used in this study starts from 2 mM , and the maximum reduction percentage using this concentration is above the LD. Therefore the feasibility of the method is confirmed, and together with the R^2 of the calibration curve and the residual plot.

5.3.2. Raw material - Heavy Metals Removal Percentage Studies

To understand whether the extraction protocol plays an important role in the adsorption process. This is due to that the treatment removes the extractive and inorganic content. A batch study using the raw material (biomass) was performed. Figure 16 indicates the percentage of reduction of copper ions at an initial concentration of 10 mM . The results indicate as expected the complete biomass was not able to remove. The reduction is exhibited by F17 and F25 when the mass is increased however statistically it is not reliable. RSD is greater than 5%, indicating that these data have high variability and may be due to error, and not by the property of the material at all. Figure 17 show SEM graph of the raw material.

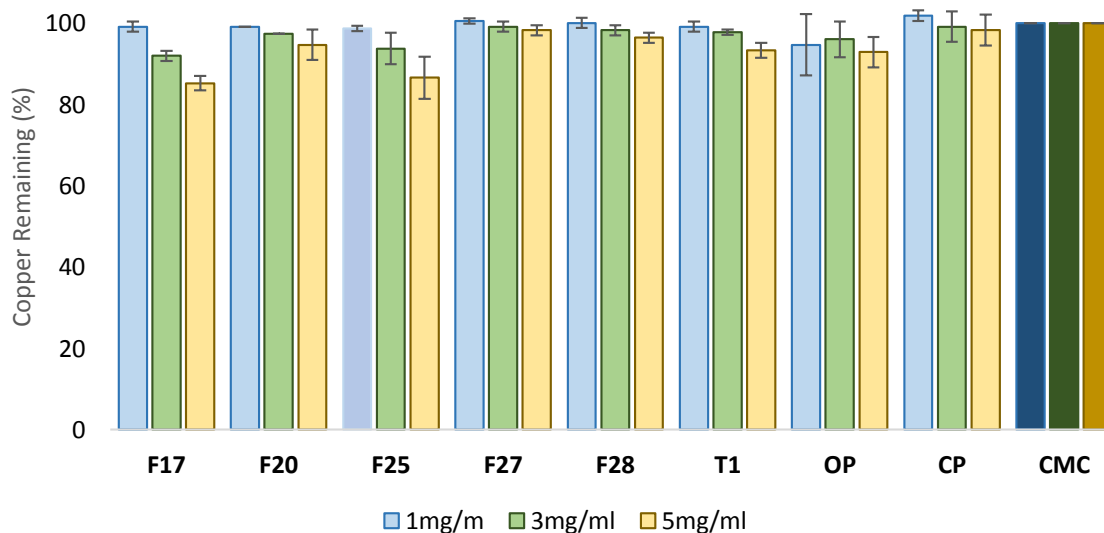


Figure 16. Percent of reduction of Cu^{2+} ions at high concentration (10 mM), using the raw materials.

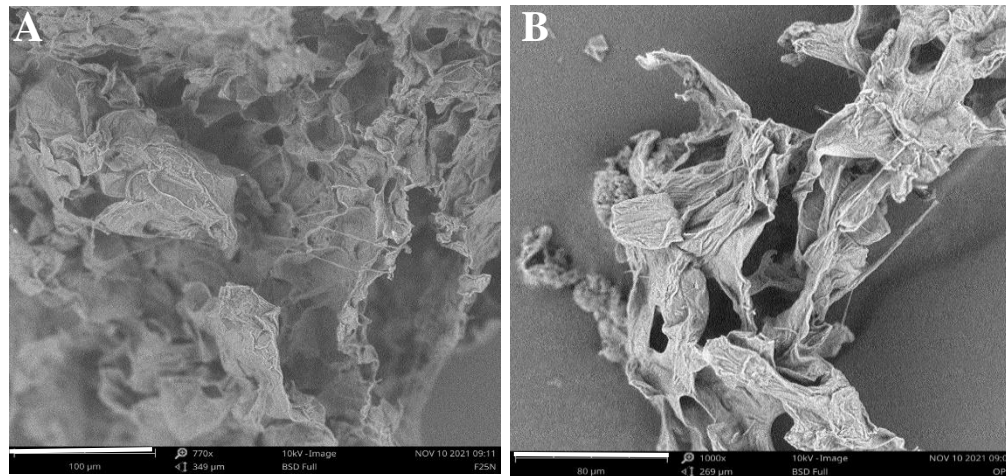


Figure 17. SEM graph as raw material for (A) F25, and (B) OP.

A SEM characterization was performed to understand the surface morphology of the raw material (Figure 17). The SEM image clearly shows a different surface with respect to the SEM image after treatment in Figure 12. F25 shows, a rougher and has many irregularities on the surface, this can be explained by the lignocellulose content before the cellulose extraction process. OP shows no porous surface, but it appears after the purification process. This result indicates that a complete surface transformation by the cellulose extraction process enhances the adsorption behavior.

5.3.3. Cellulose - Heavy Metals Removal Percentage Studies

In order to investigate which samples shows an adsorption property, batch studies were performed under fixed conditions. At low concentration (2mM), the isolates F17, F20, F25, F27, F28, T1, OP and CP show adsorption capacities of $52,54 \pm 1,15\%$, $57,62 \pm 5,48\%$, $88,75 \pm 2,49\%$, $37,30 \pm 2,96\%$, $34,84 \pm 5,60\%$, $44,35 \pm 6,03\%$, $88,45 \pm 1,70\%$, $45,31 \pm 4,03\%$, respectively (Figure 18). Results, suggested that at low concentration all samples show a quite adsorption capacity. Nevertheless, the relative standard deviation (RSD) reveals that the data for F17, F25 and OP are more confident.

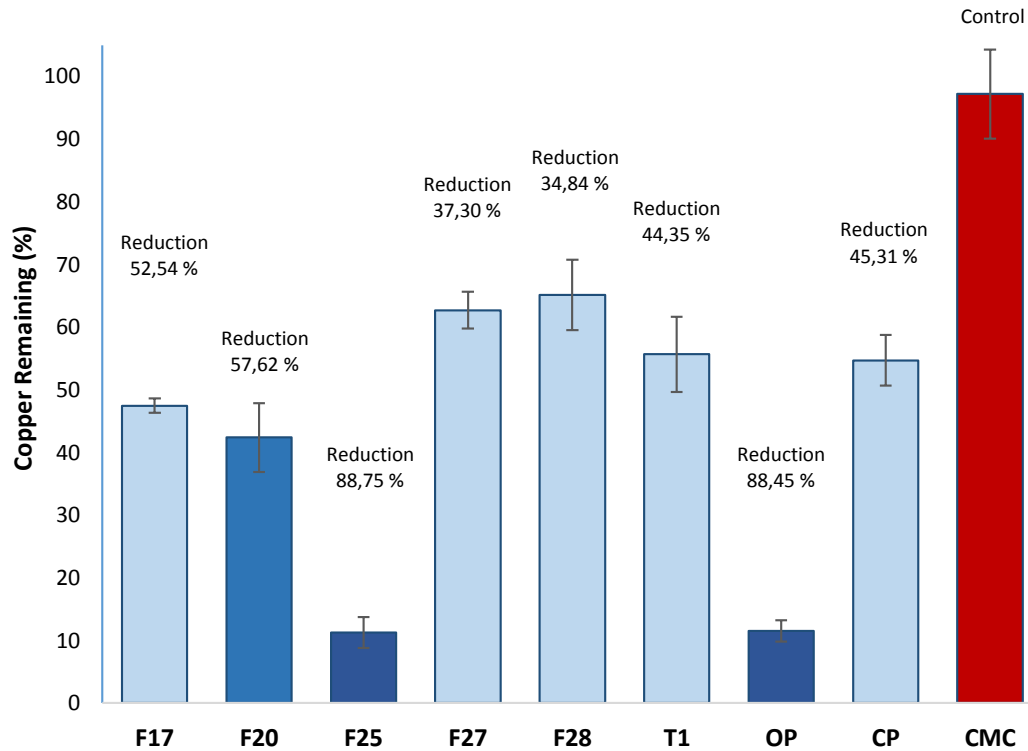


Figure 18. Percent of reduction of copper ions (2mM) after treatment with control and natural cellulose using 5mg/ml.

Results of the adsorption test at high concentration (10mM) can be observed in figure 19. According to these findings, F17, F25, and OP demonstrated an important reduction capacity than other samples. These samples were capable of removing copper ions in $37,44 \pm 1,54$, $96 \pm 2,51$ and $40,72 \pm 1,47$, respectively. The other samples show a specific removal capacity; nevertheless, the significance of these values is further analyzed in the statistical section.

Adsorption test results at 2mM and 10mM using different sorbent amounts (1mg/, 3mg/l and 5mg/L) are presented in figure 20 and figure 21, respectively. The different dose of the material is represented by the color as follows: 1 mg/ml blue, 3mg/ml as green, and orange for 5 mg/l. The highlighting color indicates the remarkable reduction percentage of heavy metal ions at each dose. These results clearly show a tendency to increase the removal percentage when the sorbent dose increases. This could be explained by the fact that more amount of mass increases the available active sites to interact with the adsorbate⁷¹. However, it does not occur in the capacity of removal expressed in q_e since the same amounts of metal ions are distributed to the more sorbent mass.

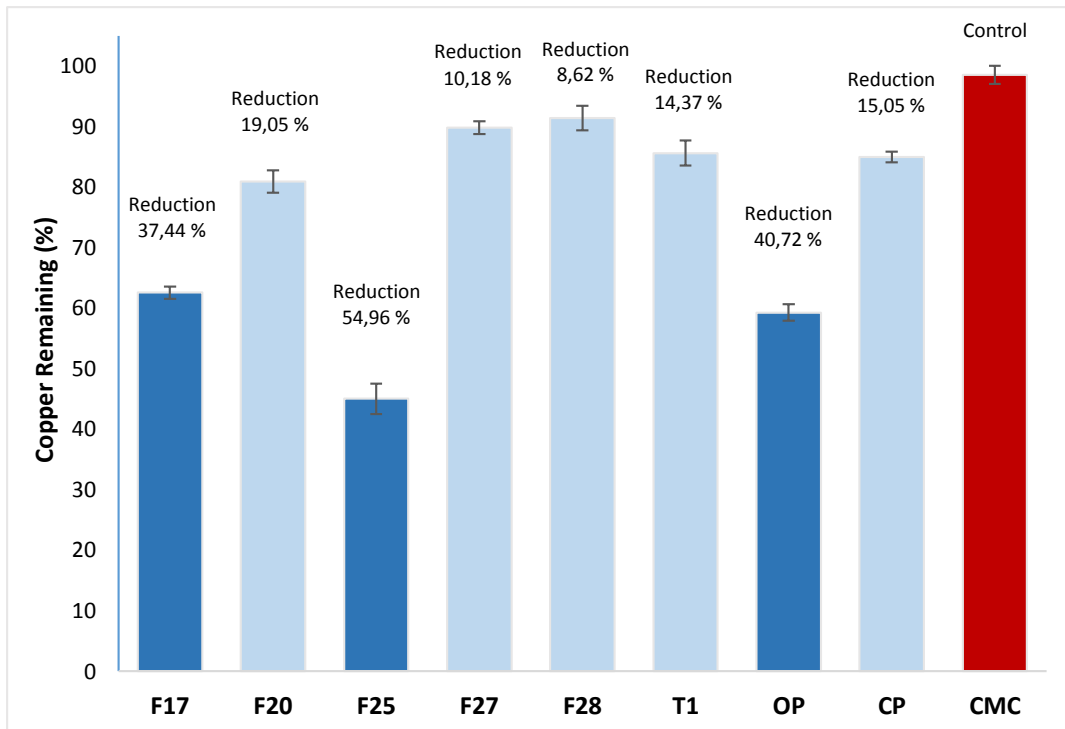


Figure 19. Percent of reduction of copper ions (10mM) after treatment with control and natural cellulose using 5mg/ml.

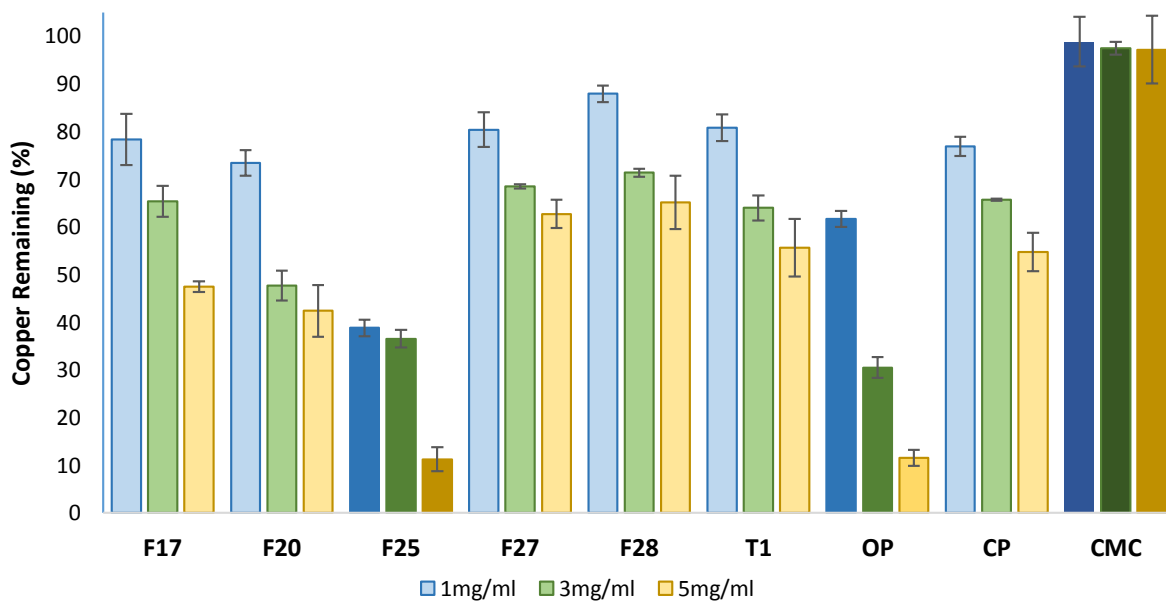


Figure 20. Percent of reduction of Cu^{2+} ions at low concentration (2mM), using three different mass (1mg/ml, 3mg/ml 5mg/ml).

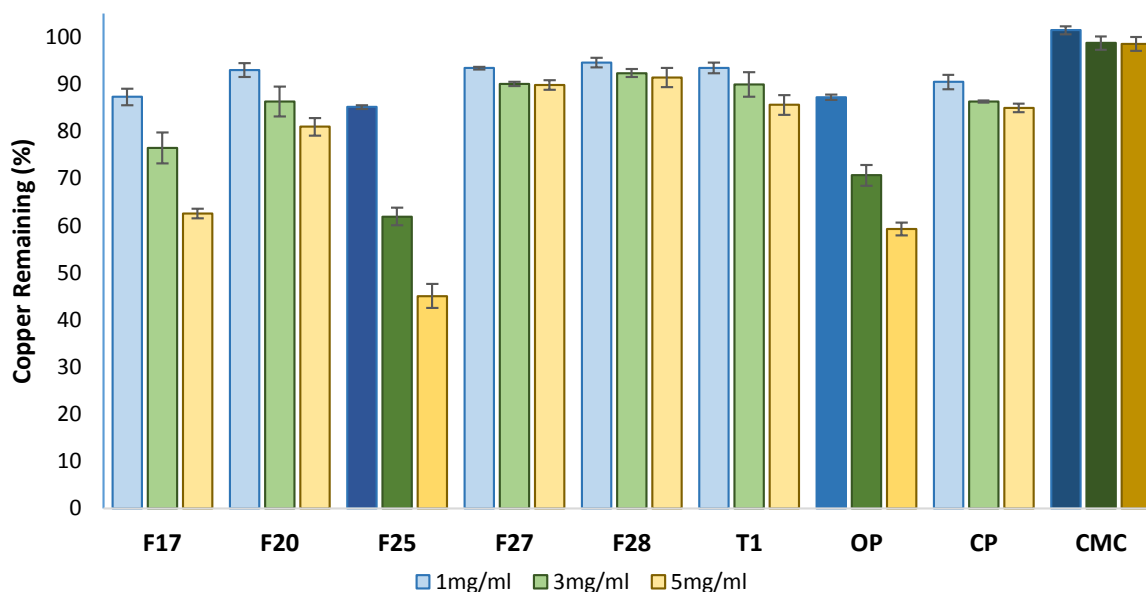


Figure 21. Reduction percentage of Cu^{2+} ions at high concentration (10mM), using three different mass (1mg/ml, 3mg/ml 5mg/ml).

5.4. Brunauer- Emmett-Teller

The BET multipoint method was employed to determine adsorbent surface area and pore size. This method used nitrogen physisorption adsorption and desorption mechanism on the surface. On the one hand, the BET surface was between $0,2 \text{ m}^2/\text{g}$ and $1,3 \text{ m}^2/\text{g}$. The result in table 7 indicates T1 and OP present a higher SSA area corresponding to $1,3 \text{ m}^2/\text{g}$ and $1 \text{ m}^2/\text{g}$, respectively. On the other hand, the pore volume was between $0,3 \text{ cc}/\text{g}$ and $1,4 \text{ cc}/\text{g}$. OP and T1 present high pore volume, $1,2 \text{ cc}/\text{g}$, and $1,4 \text{ cc}/\text{g}$, respectively. It represents around two times less than the control. All these values correspond to the porous radius until 11 nm .

Table 7. Pore volume, sample surface area, and crystallinity index of samples.

Source	SSA (m^2/g)	PV (cc/g) $\times 10^{-3}$	CrI (%)
CMC	1,447	2,986	61,4
F17	0,800	0,795	30,8
F20	0,284	0,396	50,3
F25	0,506	0,627	42,8
F27	0,975	1,130	36,4
F28	1,041	1,189	49,2
T1	1,380	1,498	48,8
OP	1,010	1,210	30,4
CP	0,428	0,662	42,5

Figure 22 shows a correlation graph between SSA and PV. All samples show lower surface area and pore volume concerning the control. The differences between the OP and F25 are in concordance with SEM images linked to irregularities in surface morphology and porosity. Considering that a higher area gives more available adsorption sites, it can assume that the T1 sample can perform better. Nevertheless, other parameters can promote adsorption⁶⁶. Table 7 summarizes the result, including CrI.

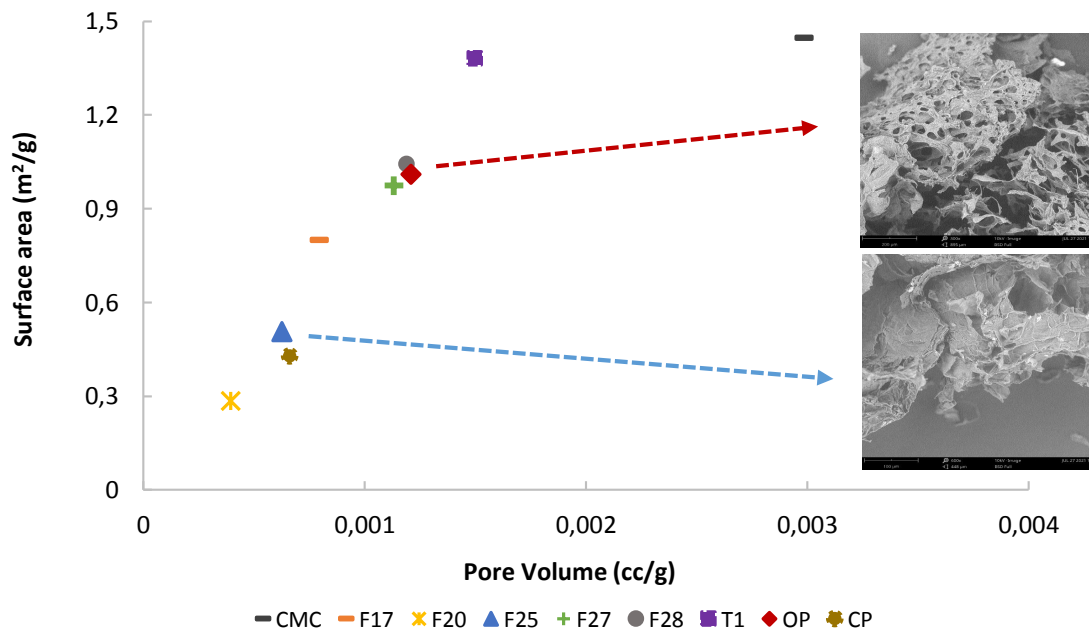


Figure 22. Distribution of the SSA correlated to the PV of the samples and the control

Results suggest adsorption capacities highlight no direct correlation of the SSA and PV, Nevertheless, according to our previous work the surface is the great important in the sorption process⁵³, suggesting that the BET measurement could have error.

5.5. Elemental composition analysis

Figure 23 shows the SEM images of the extracted samples before the adsorption test and after the adsorption test. It can be observed a change in the surface to rougher. Furthermore, it can be seen that the surfaces morphology becomes more uniform after absorption.

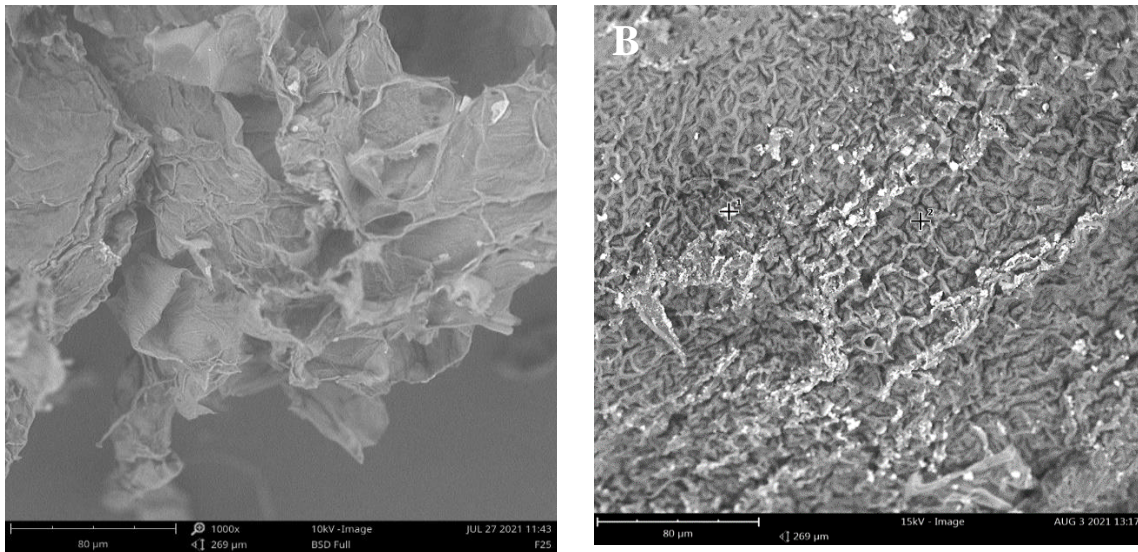


Figure 23. SEM image of F25 cellulose: (A) before and (B) after adsorption.

In order to confirm the copper ions adsorption onto the F25 surface, EDS analysis was performed. During the EDS measurement, an area of $12\ \mu\text{m} \times 9\ \mu\text{m}$ was focused and mapped. It is shown in figure 24. According to the analyzed area, the results reveal the main cellulose element composition (carbon and oxygen) and the presence of copper.

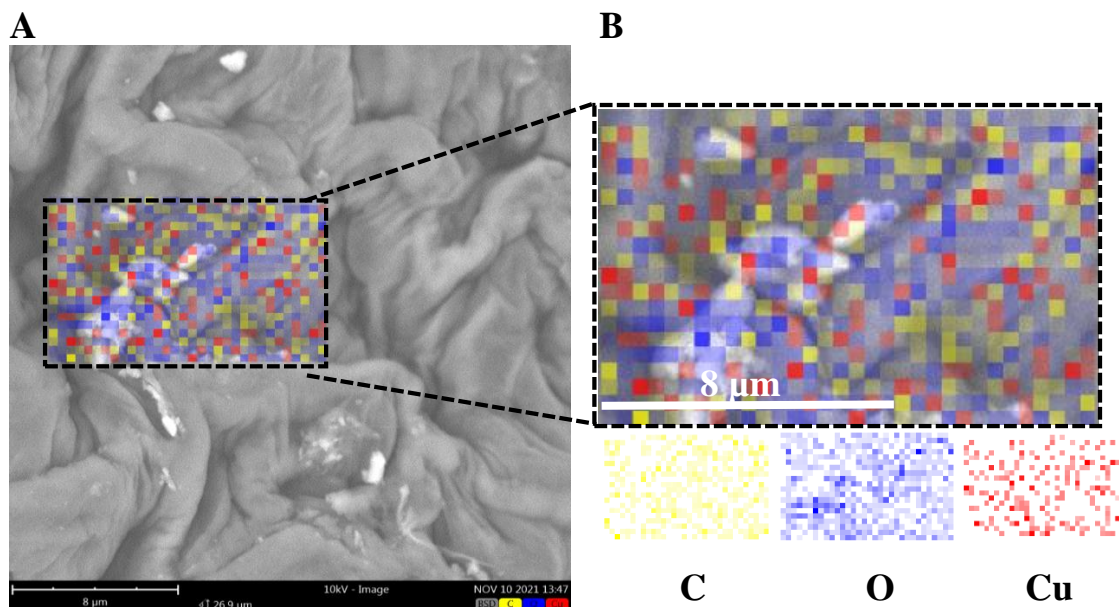


Figure 24. F25 elemental analysis after reaction with Cu^{2+} solutions (map resolution 32×20 pixel).

Figure 25 shows the spectrum where a peak for copper appears, and the quantity of C, O, and Cu is 36,8, 46,42, and 16,99 in weight concentration, respectively. The presence of peaks corresponding to Cu ions in the spectrum strongly indicated that Cu^{2+} ions bind to the F25 surface. Details of the EDX spectra values measured in atomic, weight, and stoichiometric concentration are in figure 25.

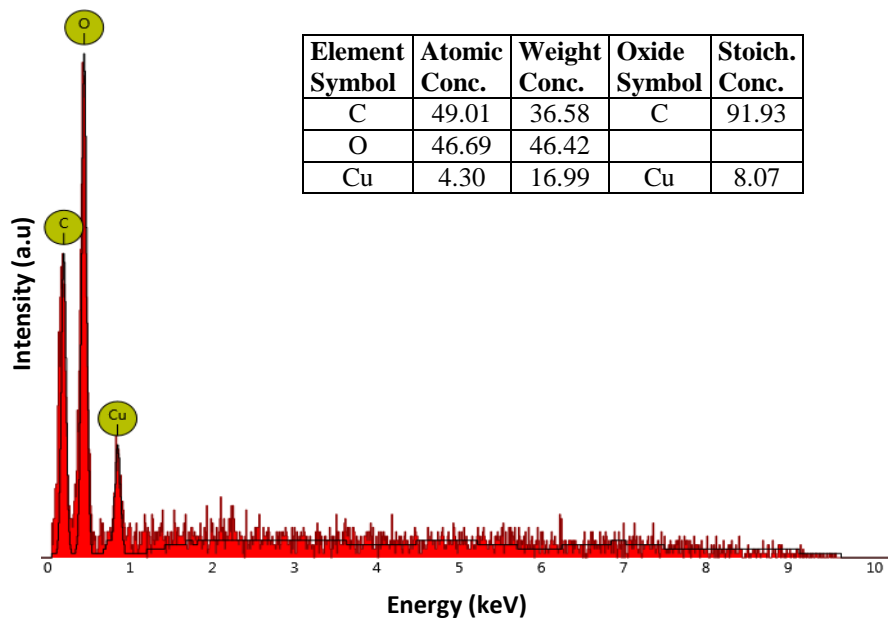


Figure 25. F25 spectrum of elemental analysis.

To confirm that not all sample exhibits a good copper ions adsorption properties, EDS analysis was performed for cellulose control and F27. Figure 26 illustrates an SEM image after the test and the composition for CMC. These analyses were performed in two spots where was no evidence of peaks corresponding to the metal ions. The found peaks correspond to carbon and oxygen. Results show C and O in 60,27, and 39,73 weight percentages, respectively. More details related to weight, atomic and stoichiometric concentration are in the table into the figure.

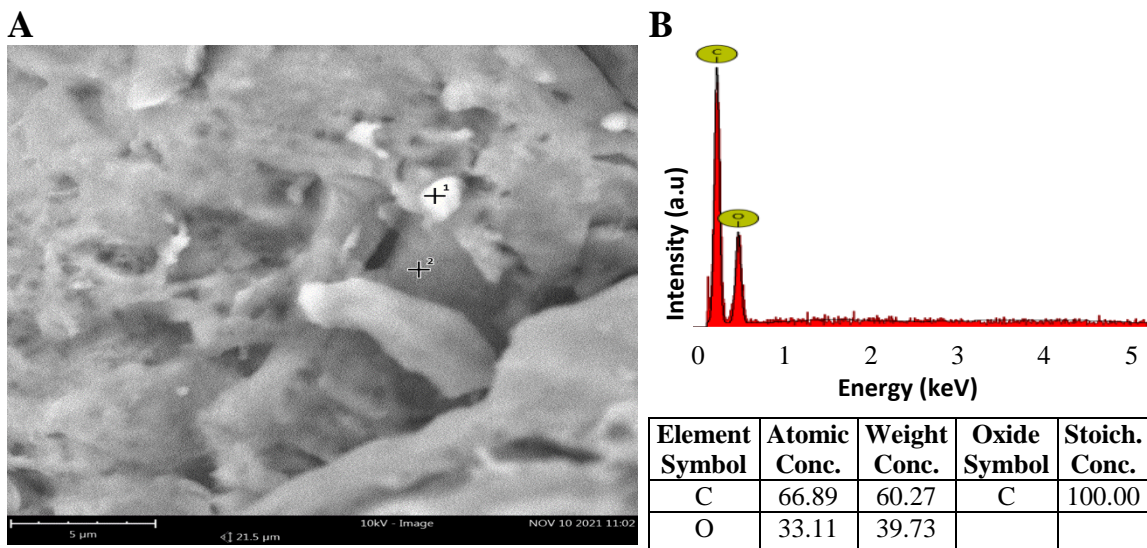


Figure 26. CMC elemental analysis after reaction, (A) SEM image with spots, and (B) spot 1 spectrum and elemental percentage.

Figure 27 indicates the SEM image of F27 after the reaction with heavy metal solutions. The analyses performed in two spots show main elemental peaks corresponding to cellulose components (C and O). Nevertheless, the result shows other elements that could be ascribed to the following reason: a) the limitations of the available EDX equipment and b) the contaminations during the experimental process ⁷².

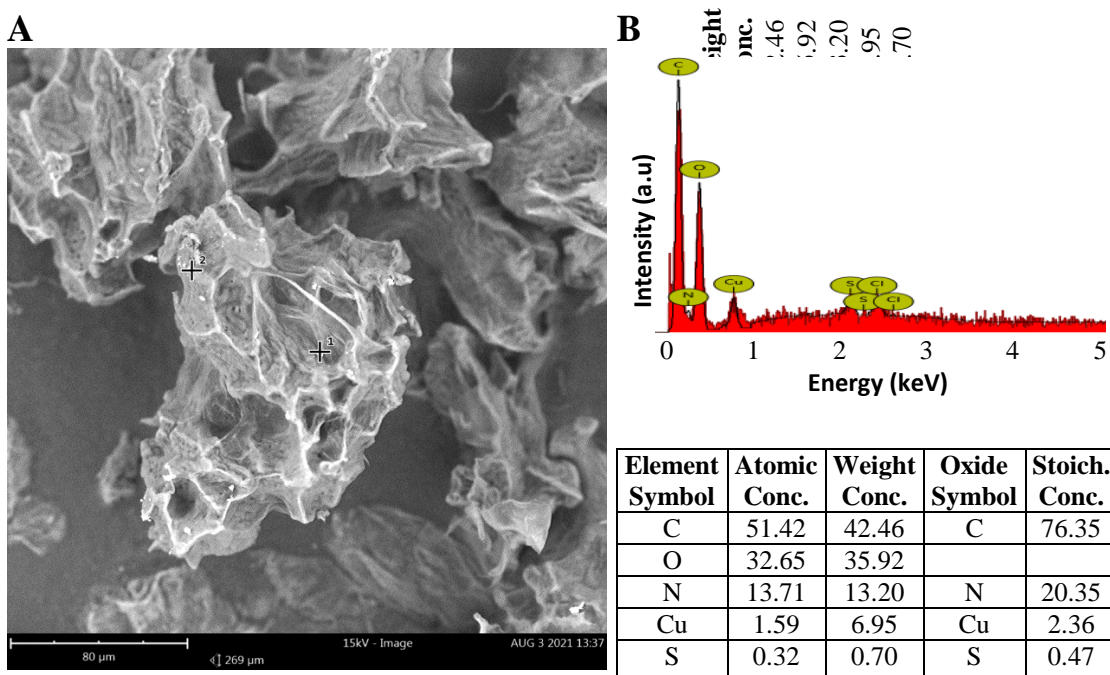


Figure 27. F27 elemental analysis after reaction, (A) SEM image with spot, and (B) spectrum and elemental percentage.

The EDS results clearly show a high amount of Cu ions on the F25 surface. While CMC does not show, copper ions and F27 indicate just a small amount. These results are in concordance with the adsorption studies since the percentage of reduction of F27 is just 10,18 %, and the reduction percentage of F25 is 54,96 % at high concentrations (10mM). These results indicate a good capacity for adsorption of F25. Furthermore, the adsorption properties related to OP and F25 could be explained by the physisorption process due to the physical characteristic found in the SEM image. However, isotherms studies could confirm prove this statement.

5.6. Isotherms studies

Two samples (F25 and OP) that have shown good adsorption behaviors were investigated to understand the interactions between the ions, surface, and maximum adsorption capacity. In this way, the results of the relationship between the equilibrium concentration (C_e) and the equilibrium removal capacity (q) were fitted to Langmuir and Freundlich adsorption isotherm models. The constant of these adsorption models could explain the material surface properties and the affinity between the adsorbate and the adsorbent.

5.6.1. F25 Langmuir and Freundlich model fitting

Langmuir Model to fit F25

The Linearized Langmuir model is widely used to fit experimental data ⁴⁶. In this context, F25 was fitted to the Langmuir model in linear and not linear forms. Figure 28 represents the data linearized by the least-squares method according to details in the methods sections. According to the linear form, the plot be $1/C_e$ vs. $1/q_e$ must follow a straight line where the slope is $1/q_m$ and the intercept is $1/(K_L q_m)$.

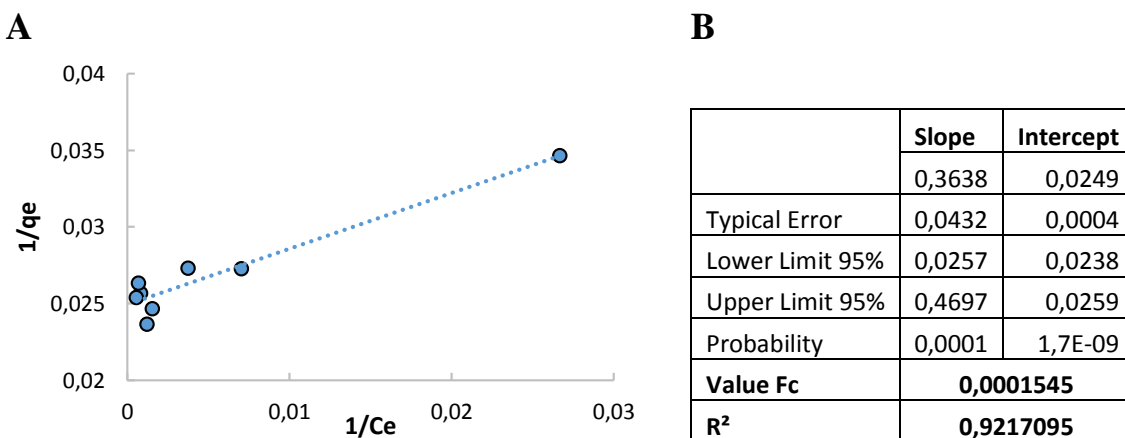


Figure 28. (A) Linear regression graph corresponds to Linearized-Langmuir function, and (B) table of covariance analysis values of F25.

The statistical values of the variance analyses of the regression are shown (Figure 28B.). According to the result, $R^2 = 0,92$ is significant since both the probability and Fc are less than 0.05, indicating that the adjustment is acceptable

Since the linear fit was significant, their parameters (q_m and K_L) were calculated and later used to fit the experimental data. The results are shown in figure 29.

To compare the linear and not linear model, the data were fit to the non-linear model using software to minimize the SSE. The result is exhibited in figure 29A. There is no difference, and it contrasts with the residual plot, which has a random distribution. In addition, linear and non-linear residual overlap, which confirms no difference.

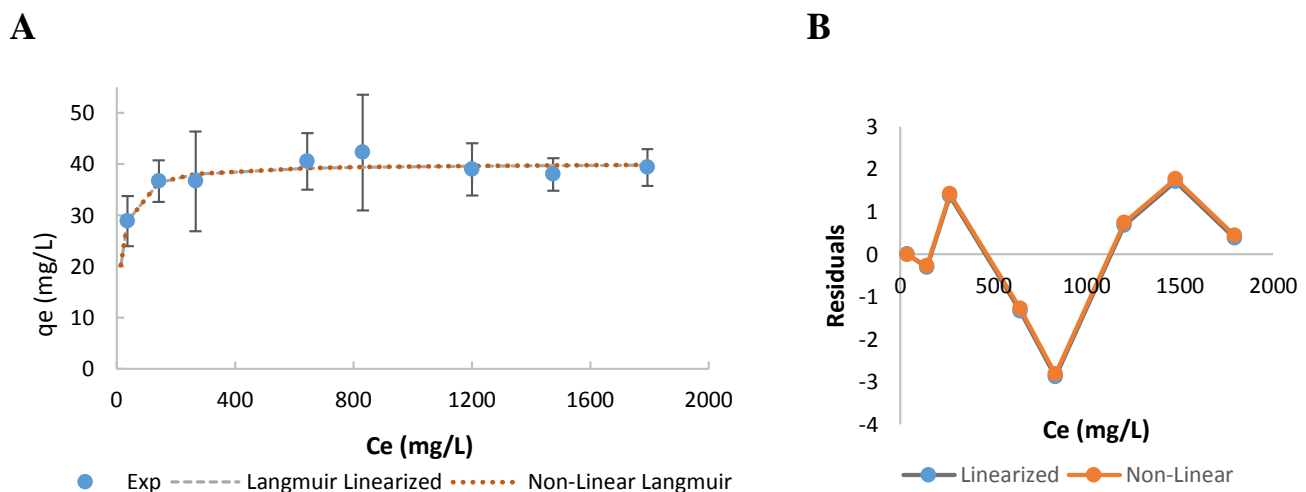


Figure 29. (A) Cu^{2+} Langmuir isotherm adsorption Linearized and not Linearized of F25 (B) and their residual respectively.

Freundlich Model to fit F25

Similarly to the previous, the data were fitted to Freundlich linear model where the linear form plot is given by $\log(C_e)$ vs $\log(q_e)$ and it must follow a straight line where the slope is $1/\text{Log}(K_F)$ and the intercept is $1/n_F$. The results are illustrated in figure 30. To verify the correct adjustment to the linear regression; variance analysis was performed, indicating that although the $R^2 = 0,70$ is lower, it is significant since the Fc is lower than the 0,05.

The compare the linear and non-linear Freundlich model, a non-linear adjustment was performed. Nevertheless, it was not impossible to find any difference since the residual distribution overlapped each other (Figure 31).

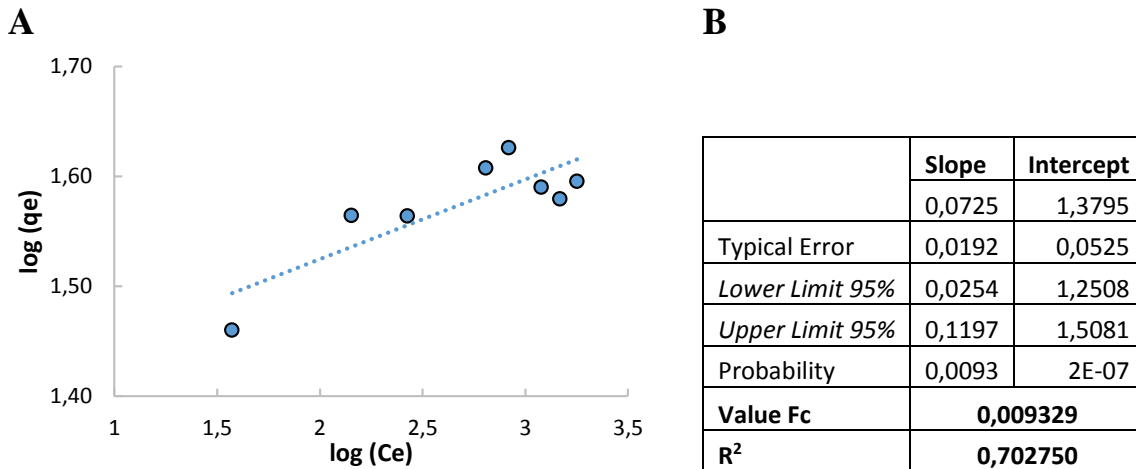


Figure 30. (A) Linear regression graph corresponds to Linearized-Freundlich function, and (B) of covariance analysis values of F25.

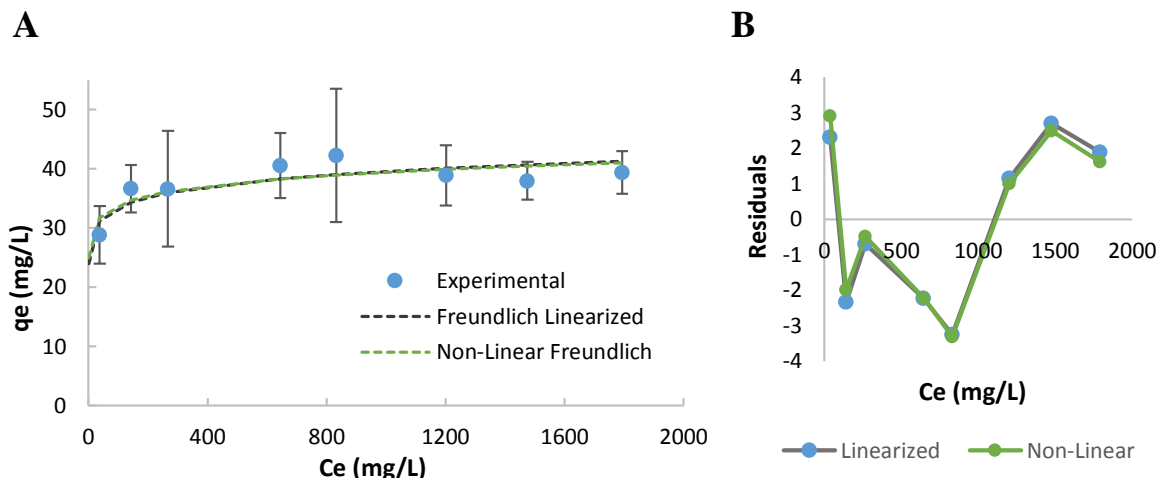


Figure 31. (A) Cu²⁺ Freundlich isotherm adsorption linearized and non-linearized of F25 (B) and their residual, respectively.

Figure 32 shows a final graph with Langmuir and Freundlich isotherms fitting. The SSE was employed to determine the best fit model, considering a lower SSE value between Langmuir and Freundlich. In addition, the equilibrium parameter (R_L) value was found in the range of 0,87 and 0,32 for the initial C_o (130 mg/L – 1900 mg/L) for Langmuir model. These values indicate that the adsorption is favorable. Although the n values, which is the coefficient of the Freundlich equation, indicate good adsorption, the correlation coefficient of the linear model suggests that the removal of copper ions fits better with the Langmuir model. According to this result, the maximum adsorption capacity for F25 was around 40 mg/g.

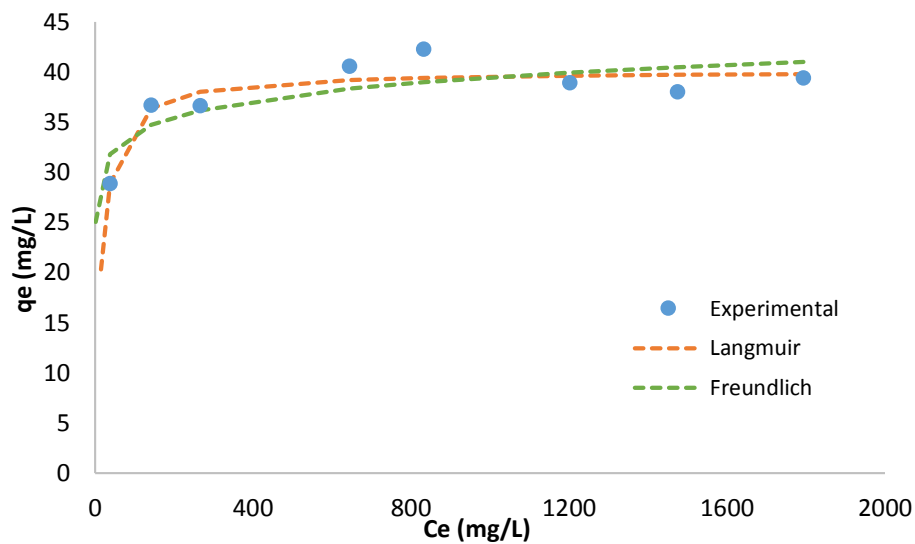


Figure 32. Experimental data fitted to Cu^{2+} ions adsorption isotherms models using F25 adsorbent.

5.6.2. OP Langmuir and Freundlich fitting

Another bio-adsorbent that demonstrated a good adsorption characteristic was OP. Therefore, it was investigated fitting the isotherm models to find approximated values to maximum adsorption capacity.

Langmuir Model to fit OP

The result of the linear fit can be found in figure 33. The Linear least-squares parameters and their statistical values are located in the table inside the figure. The critical F value implies that the $R^2 = 0,874924$ is significant. Nonetheless, this should compare with the Freundlich statistical values. Later, the non-linear fitting was performed to compare with the linear model. Figure 34 indicates that there is no difference because the respected residual plot is overlapped each other.

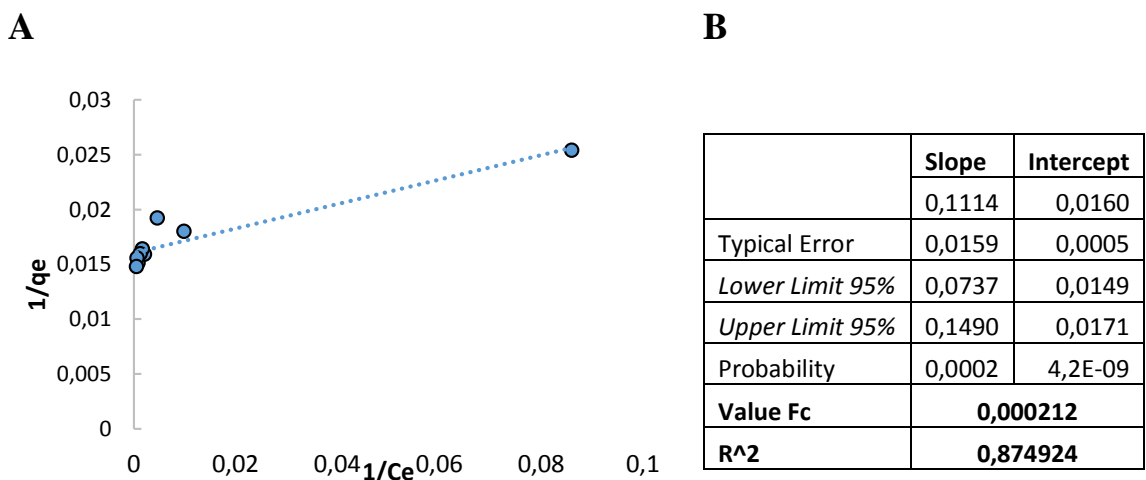


Figure 33. (A) Linear regression graph corresponds to Linearized-Langmuir model, and (B) table of covariance analysis values of OP.

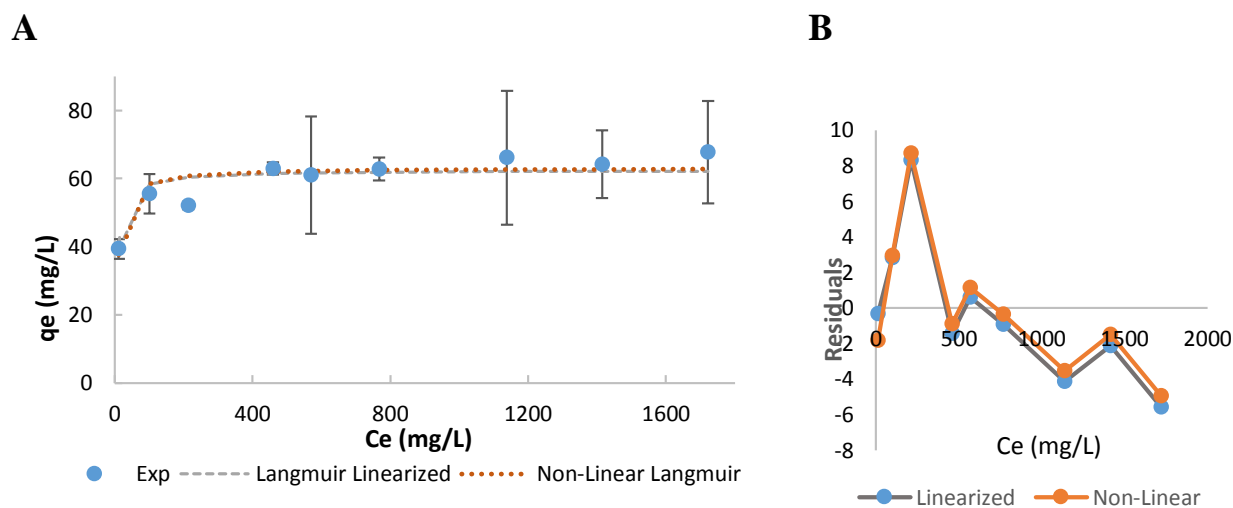


Figure 34. (A) Cu²⁺ Langmuir isotherm adsorption Linearized and not Linearized of OP, and (B) their residual respectively.

Freundlich Model to fit OP

The graph and the statistical values found exposed in figure 35 reveal that the data could fit well with the Freundlich isotherm. According to the variance analyses, the R²=0,92 is significant since the Fc is 0,000029, which gives a great linear correlation between the data.

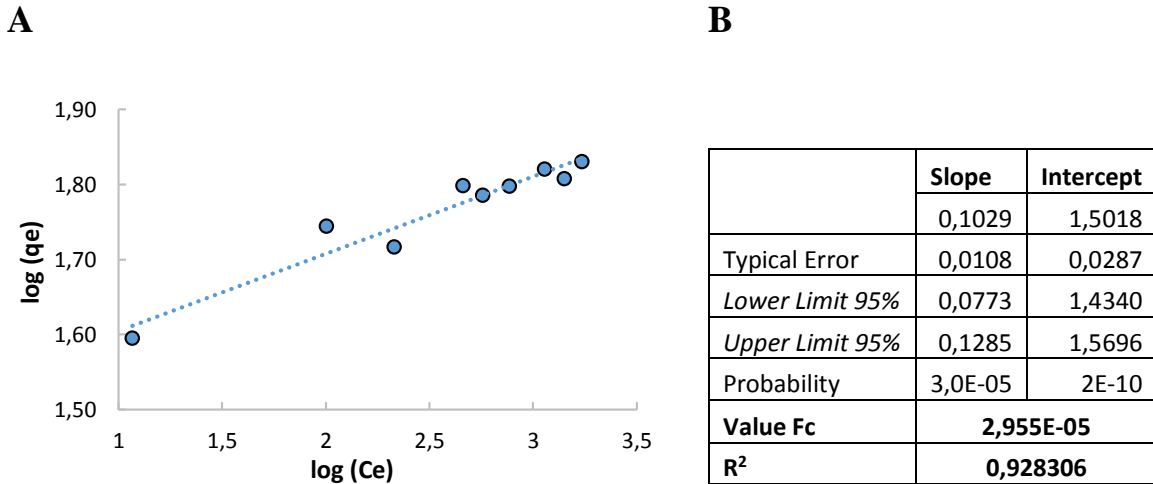


Figure 35. (A) Linear regression graph corresponds to Linearized-Freundlich function, and (B) table of covariance analysis values correspond to OP.

The non-linear fit further confirmed the applicability of the Freundlich model. The removal results of copper ions from the aqueous solution using an OP sample in a non-linear Freundlich isotherm are illustrated in figure 36. The same initial concentration as for F25 was used. The experimental data seem to fit this model, further corroborated by the residual plot. In addition, there is no significant difference between linear and no linear forms in this case.

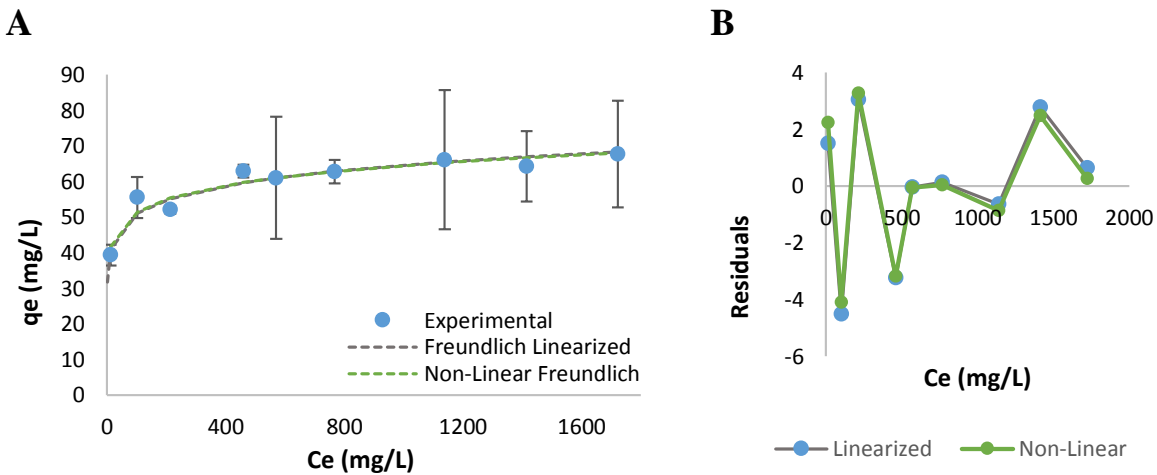


Figure 36. (A) Cu²⁺ Freundlich isotherm adsorption linearized and non-linearized of OP, and (B) their residual respectively.

The result indicated that the amount of copper ions adsorbent increased when the initial concentrations increased, but it is not proportional. Copper ions can be adsorbent until a certain amount. This process is because a high initial concentration results in more

interactions between active sites and Cu^{2+} ions. Furthermore, a high concentration of Cu^{2+} ions over the adsorbent might hasten the diffusion process³⁵. Finally, the fitted results reveal that OP tends to be a multilayer adsorbent with a maximum capacity of around 60 mg/g.

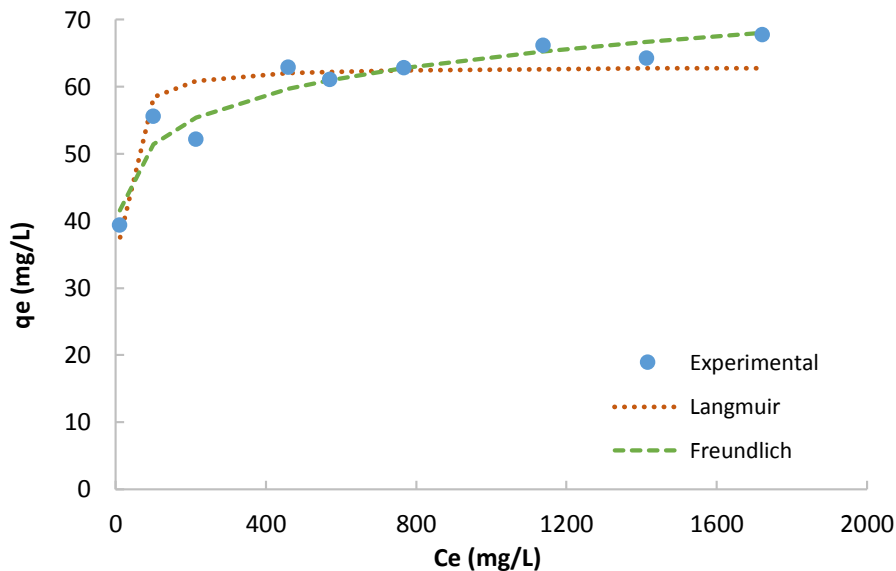


Figure 37. Experimental data fitted to Cu^{2+} ions adsorption isotherms models using OP adsorbent.

A list of the adsorption parameters and the statistical values for OP and F25 obtained from the Langmuir and Freundlich isotherms and the linearized forms, respectively, can be found in table 8. For the Linearized fit, the correlations coefficient (R^2) was used to determine the better fit, while for the non-linear model, the SSE and the residual distribution were used to determine the better fit. There is not much difference between the Linear and non-linear analysis for both models, indicating that the linear model can fit correctly. Nevertheless, it can introduce errors in the data transformation; then, the non-linear model may be used preferentially.

It can be seen that the R^2 of F25 is greater than the R^2 of OP, indicating that F25 could be well described by Langmuir isotherm. The SSE of the non-linear analysis confirms it. The SSE of Langmuir is significantly lower than Freundlich. Additionally, the statistical value R^2 for Langmuir is higher than R^2 for Freundlich in the correspond linear fit. Based on these data, Langmuir isotherm can effectively describe the adsorption behaviors of F25, indicating a monolayer and uniform adsorption on the surface.

Table 8. Isotherms parameters recovered from F25 and OP data.

Isotherm	Parameters	F25	OP
<i>Linear Langmuir</i>	qm (mg/L)	40,0981	62,3989
	KL	0,0685	0,1439
	R ²	0,9217	0,8749
<i>Linear Freundlich</i>	KF	23,9622	31,7519
	n	13,7761	9,7183
	R ²	0,7028	0,9208
<i>Non-Linear Langmuir</i>	qm (mg/L)	40,1639	63,0545
	KL	0,0681	0,1267
	SSE	15,5827	129,0790
	R ²	0,8632	0,7958
<i>Non-Linear Freundlich</i>	KF	25,0127	32,6924
	n	15,1503	10,1762
	SSE	38,2817	49,6006
	R ²	0,6642	0,9215

In the case of the OP, the R^2 of linear Freundlich is higher than linear Langmuir, indicating that OP can be described quite better by Freundlich isotherm. Another parameter that confirms that OP tends to follow a Freundlich model is the SSE. The SSE for Freundlich is much smaller than the Langmuir in non-linear models. The results show that the fit model is in concordance with the literature ⁵¹.

According to the statistical parameters, the R^2 was not able to compare the linear and non-linear forms. Since the R^2 in the linearized model is the correlations coefficient obtained from the linear regression and the variance analysis, while R^2 for the non-linear fit is obtained from the validation of the residual between experimental values and the values predicted by the model.

Figure 38 highlights a comparison between the samples fitted to the isotherms models. Although in the characterization, OP and F25 show certain similitudes in the CrI values (both have low CrI), indicating that they are formed for a great amorphous region. In the same way, during the thermal degradation profile (first derivate), these bio adsorbents show an important percentage of degradation in the second stage (200-270°C), indicating that these samples have a similar composition percentage.

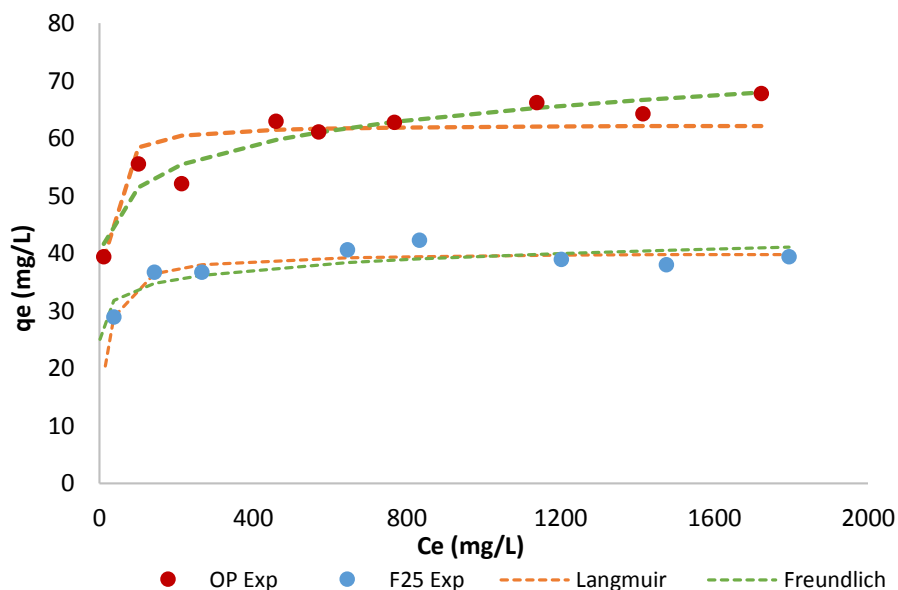


Figure 38. Cu^{2+} ions adsorption isotherms models comparison between F25 and OP extracted from the natural source

As mentioned above, the maximum capacity of adsorption was around 40 mg/g and 60 mg/g for F25 and OP, respectively. The differences in the q_m value and the good fit model for F25 and OP could be explained by SEM images. There is a significant difference in the surface morphology and porous. F25 shows a flat and less porosity while OP shows a great porosity and high SSA, giving them more area to interact and form multilayer sorption.

5.7. Statistical analysis

A full factorial design analysis was performed to prove the reduction percentage according to method sections. Table 9 shows the result of the FFD, and it summarizes statistical values for corresponding samples and the meaning of interaction between the factors.

The intercept is the means of low levels. In this case, a concentration of 2mM and mass of adsorbed corresponding to 1mg/ml for CMC. The result of a complex model, which includes a third level interaction, shows that the third interaction was not significant, the reason why the model was reduced only for the exchange of the second level. All samples show substantial differences concerning to the control, which implies that the samples reduction percentage was acceptable. F25 and OP, as expected from the previous section, have shown better performance. They reflected over two times adsorption capacity to respect others.

The mass and concentration do not exhibit a level of significance. This implies that when mass or concentration is changed, the material behaviors are the same. The percentage of reduction could change, but the samples work in the same way for both concentrations. The concentration variation could not affect, but there is an interaction between the material and the aqueous solution concentration, indicated by the significant codes. There is an inverse relationship between the material and the concentration, indicating that the percentage of the reduction decreases when concentration increases. This is exhibited in the table as a negative value. It could be explained because of the sample surface saturation. The result indicated that the material has a saturation point and it is in the concentration range used in this work. In addition, it is important to mention that the interaction between the F17 and the concentration is not significant also the CP interaction with the mass.

Table 9. Statistical values of the full factorial design.

	Estimate Std	Error	t value	Pr (> t)	Significant
(Intercept)	2.164	2.766	0.782	0.44318	
CP	32.086	3.911	8.204	7.89e-08	***
F17	34.128	3.911	8.726	2.97e-08	***
F20	43.327	3.911	11.078	5.51e-10	***
F25	68.963	3.911	17.632	1.18e-13	***
OP	63.257	3.911	16.173	5.96e-13	***
T1	31.018	3.911	7.931	1.33e-07	***
Mass	3.544	2.560	1.384	0.18157	
Con	-1.739	3.911	-0.445	0.66139	
CP:Mass	5.787	3.387	1.709	0.10301	
F17:Mass	12.768	3.387	3.769	0.00121	**
F20:Mass	9.659	3.387	2.852	0.00986	**
F25:Mass	15.788	3.387	4.661	0.00015	***
OP:Mass	18.391	3.387	5.429	2.58e-05	***
T1:Mass	7.115	3.387	2.100	0.04857	*
CP:Con	-19.763	5.531	-3.573	0.00190	**
F17:Con	-9.994	5.531	-1.807	0.08585	.
F20:Con	-30.499	5.531	-5.514	2.13e-05	***
F25:Con	-33.412	5.531	-6.041	6.63e-06	***
OP:Con	-36.073	5.531	-6.522	2.34e-06	***
T1:Con	-21.102	5.531	-3.815	0.00108	**
Mass:Con	-4.824	1.811	-2.664	0.01489	*

*** = 0,001 ** = 0,01 * = 0,05 . = 0,1

The equation 10 was found from the significant values of the samples and their interactions with the mass and concentration. According to the result in table 9, the mass, concentration, interaction between the F17 and concentration, and CP interaction with mass are not

significant. Therefore, it is not included in the final equation. This equation describes a function to obtain a removal percentage value under the given conditions.

$$\begin{aligned}
 Y = & 2,164 + 34,128CP + 43,327F20 + 68,963F25 + 63,257OP + 31,018T1 \quad (10) \\
 & + 12,768F17 * B + 9,659 F20 * B + 15,788F25 * B \\
 & + 18,391OP * B + 7,115T1 * B - 19,763CP * C - 9,994F17 \\
 & * C - 30,499F20 * C - 33,412F25 * C - 36,073OP * C \\
 & - 21,102T1 * C - 4B * C
 \end{aligned}$$

Some predicted values using the mentioned model were calculated and summarized in table 10. The results indicate that the function predicts well. It was further validated with the parameters of the residual found in figure 39. The residual plot follows a random distribution and it associated to normal residual histogram. In addition, it was corroborated with the statistical parameters of the model, indicating a good adjustment of the function to experimental data.

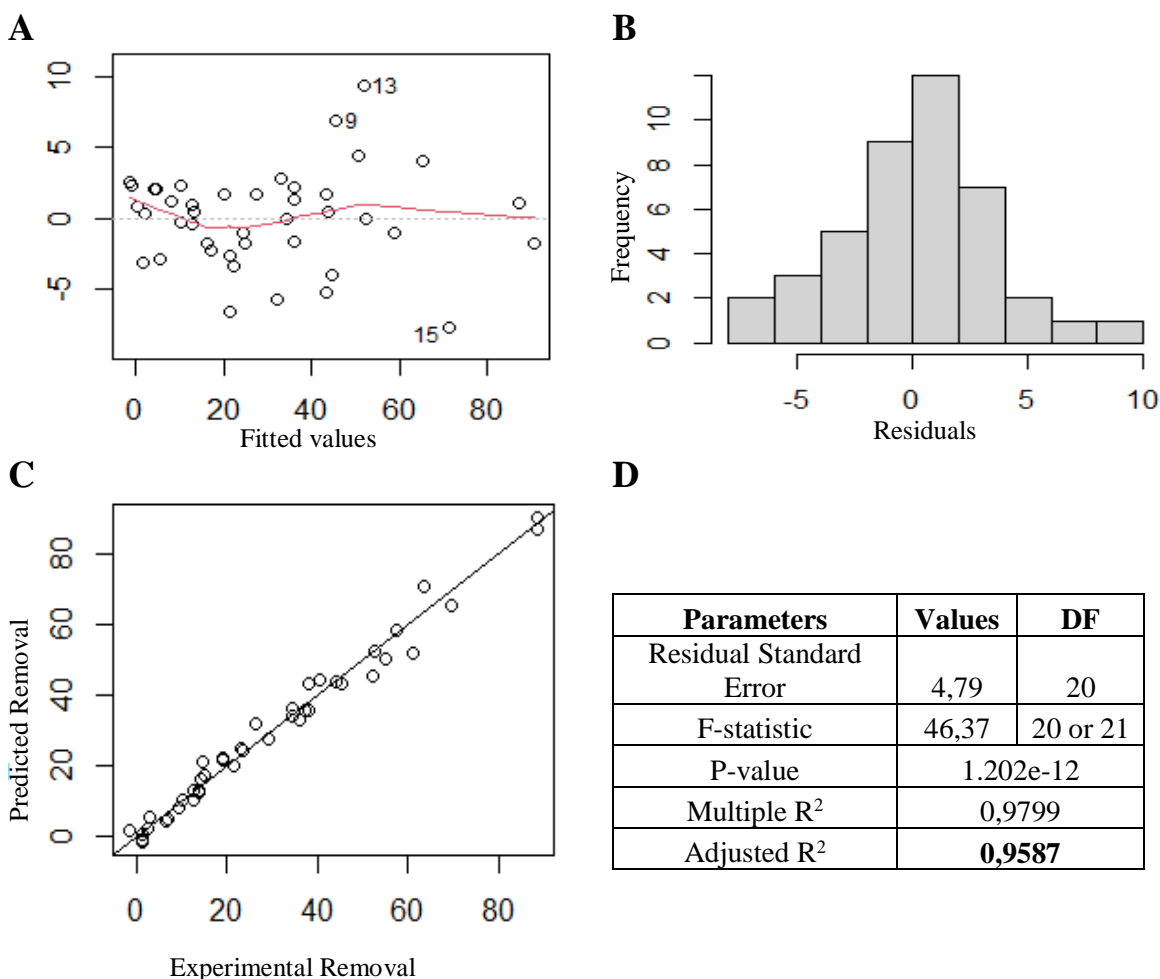


Figure 39. (A) Residual random distribution plot, (B) residual histogram, (C) regression of experimental and predicted values and (D) statistical parameters values.

Table 10. Some predicted values of OP and F25

Samples	Mass	Concentration	Experimental	Predicted
OP	1	1	40,72	42,915
OP	0	1	29,34	29,348
OP	1	0	88,45	83,812
F25	1	1	54,96	48,679
F25	0	1	38,12	37,715
F25	1	0	88,75	86,915

Chapter 6

Conclusion & Outlook

In this present work, eight unmodified celluloses from Ecuadorian plant biodiversity were successfully isolated. Rigorous, physicochemical characterization was performed on the isolated cellulose samples using FTIR, XRD, SEM, TGA, and BET, indicating that the source directly affects their characteristic. F17 and OP show low crystallinity degrees, whereas F17, F25, and OP exhibit similar thermal degradation profiles. These properties are directly correlated since low CrI indicates that the samples are composed of a great amorphous region, and it is a critical factor that significantly affects the metal ions adsorption.

The heavy metals ions adsorption test was performed effectively, highlighting that F25 and OP demonstrate better Cu^{2+} ions adsorption due to their amorphous structure, which increases the surface area. Later, EDS analysis confirmed the Cu^{2+} adsorption, which was contrasted to the CMC, which does not show adsorption capacities. Since some samples show similitudes in the characteristic such *CrI* nevertheless reveals different adsorption capacity, their unique physicochemical properties could play a critical role in the sorption process. Furthermore, according to the TGA profile certain amount of the hemicellulose content could influence during adsorption of heavy metals.

Additionally, F25 fit better to the Langmuir adsorption model, whereas OP fits better to the Freundlich model. It could be explained by the SEM image since OP shows a great porosity and large surface area that allows a multilayer formation, and F25 exhibits a monolayers ions deposition. The maximum capacity of Cu^{2+} ions adsorption was around 40 mg/g and 60 mg/g for F25 and OP, respectively. Finally, this work demonstrates that the intrinsic physicochemical properties are directly associated with the Ecuadorian material source in order to generate particular cellulose-based material as an alternative for effective water treatment.

For future work, more studies must be done to understand better the material capacity and adsorption mechanism. These studies could include a change in reaction conditions, for instance, pH and temperature. The rate of the reaction could be studied throughout kinetic studies. Moreover, the sample must be test using another metals ion. Additionally, a PEI-functionalization could be performed to enhance the adsorption capacity. Finally, the BET result differs from our published work; therefore, it requires repeating the experiment to better explain the adsorption process and efficiency.

References

1. Vareda, J. P., Valente, A. J. M. & Durães, L. Assessment of heavy metal pollution from anthropogenic activities and remediation strategies: A review. *Journal of Environmental Management* **246**, 101–118 (2019).
2. Fu, F. & Wang, Q. Removal of heavy metal ions from wastewaters: A review. *Journal of Environmental Management* **92**, 407–418 (2011).
3. Qasem, N. A. A., Mohammed, R. H. & Lawal, D. U. Removal of heavy metal ions from wastewater: a comprehensive and critical review. *npj Clean Water* **4**, (2021).
4. Panagos, P., Van Liedekerke, M., Yigini, Y. & Montanarella, L. Contaminated sites in Europe: Review of the current situation based on data collected through a European network. *Journal of Environmental and Public Health* **2013**, (2013).
5. Cipriani-Avila, I. *et al.* Heavy metal assessment in drinking waters of Ecuador: Quito, Ibarra and Guayaquil. *Journal of Water and Health* **18**, 1050–1064 (2020).
6. Stern, B. R. Essentiality and toxicity in copper health risk assessment: Overview, update and regulatory considerations. *Journal of Toxicology and Environmental Health - Part A: Current Issues* **73**, 114–127 (2010).
7. Organization, W. H. *Copper Environmental Health Criteria 200*. (IPCS, WHO, 1998).
8. Mautner, A. *et al.* Natural fibre-nanocellulose composite filters for the removal of heavy metal ions from water. *Industrial Crops and Products* **133**, 325–332 (2019).
9. Assurance, U. S. E. A. and C. *Nationl Primary Drinking Water Regulations*. (U.S Environmental Protection Agency adn Compliance Assurance, 2013).
10. World Health Organization & WHO, S. *Guidelines for drinking-water quality (Vol.1)*. (2004).
11. Wen, T., Qu, F., Li, N. B. & Luo, H. Q. A facile, sensitive, and rapid spectrophotometric method for copper(II) ion detection in aqueous media using polyethyleneimine. *Arabian Journal of Chemistry* **10**, S1680–S1685 (2017).
12. Guerra, F. D., Attia, M. F., Whitehead, D. C. & Alexis, F. Nanotechnology for environmental remediation: Materials and applications. *Molecules* **23**, 1–23 (2018).
13. Bethke, K. *et al.* Functionalized Cellulose for Water Purification, Antimicrobial Applications, and Sensors. *Advanced Functional Materials* **28**, 1–14 (2018).
14. Carpenter, A. W., De Lannoy, C. F. & Wiesner, M. R. Cellulose nanomaterials in water treatment technologies. *Environmental Science and Technology* **49**, 5277–5287 (2015).
15. Pineda, E. P., Guaya, D., Tituana, C., Osorio, F. & García-Ruiz, M. J. Biochar from agricultural by-products for the removal of lead and cadmium from drinking water. *Water (Switzerland)* **12**, 1–16 (2020).
16. Santos, B. M. *et al.* Determinación de cadmio y plomo en agua, sedimento y organismos bioindicadores en el Estero Salado, Ecuador. *Enfoque UTE* **9**, 89–105 (2018).
17. Choudhury, R. R., Sahoo, S. K. & Gohil, J. M. Potential of bioinspired cellulose

- nanomaterials and nanocomposite membranes thereof for water treatment and fuel cell applications. *Cellulose* **27**, 6719–6746 (2020).
18. Klemm, D., Heublein, B., Fink, H. P. & Bohn, A. Cellulose: Fascinating biopolymer and sustainable raw material. *Angewandte Chemie - International Edition* **44**, 3358–3393 (2005).
 19. George, J. & Sabapathi, S. N. Cellulose nanocrystals: Synthesis, functional properties, and applications. *Nanotechnology, Science and Applications* **8**, 45–54 (2015).
 20. Gibson, L. J. The hierarchical structure and mechanics of plant materials. *Journal of the Royal Society Interface* **9**, 2749–2766 (2012).
 21. Greis, K. *et al.* One-Pot Synthesis of Xanthate-Functionalized Cellulose for the Detection of Micromolar Copper(II) and Nickel(II) Ions. *Clean - Soil, Air, Water* **47**, 1–4 (2019).
 22. Ma, H., Hsiao, B. S. & Chu, B. Ultrafine cellulose nanofibers as efficient adsorbents for removal of UO₂²⁺ in water. *ACS Macro Letters* **1**, 213–216 (2012).
 23. Badgar, K., Abdalla, N., El-Ramady, H. & Prokisch, J. Sustainable Applications of Nanofibers in Agriculture and Water Treatment: A Review. *Sustainability (Switzerland)* **14**, 1–17 (2022).
 24. Saravanan, R. & Ravikumar, L. Cellulose bearing Schiff base and carboxylic acid chelating groups: A low cost and green adsorbent for heavy metal ion removal from aqueous solution. *Water Science and Technology* **74**, 1780–1792 (2016).
 25. Rahman, N. S. A., Yhaya, M. F., Azahari, B. & Ismail, W. R. Utilisation of natural cellulose fibres in wastewater treatment. *Cellulose* **25**, 4887–4903 (2018).
 26. Varghese, A. G., Paul, S. A. & Latha, M. S. Remediation of heavy metals and dyes from wastewater using cellulose-based adsorbents. *Environmental Chemistry Letters* **17**, 867–877 (2019).
 27. Setyono, D. & Valiyaveetil, S. Functionalized paper-A readily accessible adsorbent for removal of dissolved heavy metal salts and nanoparticles from water. *Journal of Hazardous Materials* **302**, 120–128 (2016).
 28. Chong, H. L. H., Chia, P. S. & Ahmad, M. N. The adsorption of heavy metal by Bornean oil palm shell and its potential application as constructed wetland media. *Bioresource Technology* **130**, 181–186 (2013).
 29. Hossain, M. A., Ngo, H. H., Guo, W. S. & Nguyen, T. V. Palm oil fruit shells as biosorbent for copper removal from water and wastewater: Experiments and sorption models. *Bioresource Technology* **113**, 97–101 (2012).
 30. Sobhanardakani, S., Parvizimosaed, H. & Olyaie, E. Heavy metals removal from wastewaters using organic solid waste-rice husk. *Environmental Science and Pollution Research* **20**, 5265–5271 (2013).
 31. Feng, N. C., Guo, X. Y. & Liang, S. Enhanced Cu(II) adsorption by orange peel modified with sodium hydroxide. *Transactions of Nonferrous Metals Society of China (English Edition)* **20**, s146–s152 (2010).
 32. Zamora-Ledezma, C. *et al.* Heavy metal water pollution: A fresh look about hazards, novel and conventional remediation methods. *Environmental Technology and Innovation* **22**, 101504 (2021).
 33. Amoatey Peace, B. R. *Wastewater Management. Waste Water - Evaluation and Management* vol. 130 (2011).
 34. Phuong, H. T., Thoa, N. K., Tuyet, P. T. A., Van, Q. N. & Hai, Y. D. Cellulose Nanomaterials as a Future, Sustainable and Renewable Material. *Crystals* **12**, (2022).

35. Li, C. & Removal, I. High-Performance Hydrogel Adsorbent Based on Cellulose . (2021).
36. Miran, W. *et al.* Mixed sulfate-reducing bacteria-enriched microbial fuel cells for the treatment of wastewater containing copper. *Chemosphere* **189**, 134–142 (2017).
37. Ezziat, L., Elabed, A., Ibsouda, S. & El Abed, S. Challenges of microbial fuel cell architecture on heavy metal recovery and removal from wastewater. *Frontiers in Energy Research* **7**, 1–13 (2019).
38. Armbruster, M. H. & Austin, J. B. The Adsorption of Gases on Plane Surfaces of Mica. *Journal of the American Chemical Society* **60**, 467–475 (1938).
39. Liu, P., Garrido, B., Oksman, K. & Mathew, A. P. Adsorption isotherms and mechanisms of Cu(II) sorption onto TEMPO-mediated oxidized cellulose nanofibers. *RSC Advances* **6**, 107759–107767 (2016).
40. Daochalermwong, A. *et al.* Removal of Heavy Metal Ions Using Modified Celluloses Prepared from Pineapple Leaf Fiber. *ACS Omega* **5**, 5285–5296 (2020).
41. Abdelnaeim, M. Y., El Sherif, I. Y., Attia, A. A., Fathy, N. A. & El-Shahat, M. F. Impact of chemical activation on the adsorption performance of common reed towards Cu(II) and Cd(II). *International Journal of Mineral Processing* **157**, 80–88 (2016).
42. Xu, F., Yu, J., Tesso, T., Dowell, F. & Wang, D. Qualitative and quantitative analysis of lignocellulosic biomass using infrared techniques: A mini-review. *Applied Energy* **104**, 801–809 (2013).
43. Hospodarova, V., Singovszka, E. & Stevulova, N. Characterization of Cellulosic Fibers by FTIR Spectroscopy for Their Further Implementation to Building Materials. *American Journal of Analytical Chemistry* **09**, 303–310 (2018).
44. Zhuang, J., Li, M., Pu, Y., Ragauskas, A. J. & Yoo, C. G. Observation of potential contaminants in processed biomass using fourier transform infrared spectroscopy. *Applied Sciences (Switzerland)* **10**, 1–13 (2020).
45. Kim, S. H., Lee, C. M. & Kafle, K. Characterization of crystalline cellulose in biomass: Basic principles, applications, and limitations of XRD, NMR, IR, Raman, and SFG. *Korean Journal of Chemical Engineering* **30**, 2127–2141 (2013).
46. Qin, F. *et al.* Efficient Removal of Cu²⁺ in Water by Carboxymethylated Cellulose Nanofibrils: Performance and Mechanism. *Biomacromolecules* vol. 20 (2019).
47. Poletto, M., Ornaghi Júnior, H. L. & Zattera, A. J. Native cellulose: Structure, characterization and thermal properties. *Materials* **7**, 6105–6119 (2014).
48. Girão, A. V., Caputo, G. & Ferro, M. C. Application of Scanning Electron Microscopy–Energy Dispersive X-Ray Spectroscopy (SEM-EDS). *Comprehensive Analytical Chemistry* **75**, 153–168 (2017).
49. Ambroz, F., Macdonald, T. J., Martis, V. & Parkin, I. P. Evaluation of the BET theory for the characterization of meso and microporous MOFs. *Small Methods* **2**, 1–17 (2018).
50. Gonte, R. R., Balasubramanian, K. & Mumbreakar, J. D. Porous and Cross-Linked Cellulose Beads for Toxic Metal Ion Removal: Hg(II) Ions. *Journal of Polymers* **2013**, 1–9 (2013).
51. Castro, D. *et al.* Article chemical modification of agro-industrial waste-based bioadsorbents for enhanced removal of Zn(II) ions from aqueous solutions. *Materials* **14**, (2021).
52. Segal, L., Creely, J. J., Martin, A. E. & Conrad, C. M. An Empirical Method for Estimating the Degree of Crystallinity of Native Cellulose Using the X-Ray

- Diffractionmeter. *Textile Research Journal* **29**, 786–794 (1959).
53. Bravo, I. *et al.* Cellulose particles capture aldehyde VOC pollutants. *RSC Advances* **10**, 7967–7975 (2020).
 54. Guambo, M. P. R. *et al.* Natural cellulose fibers for surgical suture applications. *Polymers* **12**, 1–20 (2020).
 55. Abidi, N., Cabrales, L. & Haigler, C. H. Changes in the cell wall and cellulose content of developing cotton fibers investigated by FTIR spectroscopy. *Carbohydrate Polymers* **100**, 9–16 (2014).
 56. El Oudiani, A., Msahli, S. & Sakli, F. In-depth study of agave fiber structure using Fourier transform infrared spectroscopy. *Carbohydrate Polymers* **164**, 242–248 (2017).
 57. Viera-Herrera, C. *et al.* Microcrystalline cellulose extracted from native plants as an excipient for solid dosage formulations in drug delivery. *Nanomaterials* **10**, 1–12 (2020).
 58. Nelson, M. L. & O'Connor, R. T. Relation of certain infrared bands to cellulose crystallinity and crystal lattice type. Part II. A new infrared ratio for estimation of crystallinity in celluloses I and II. *Journal of Applied Polymer Science* **8**, 1325–1341 (1964).
 59. Lionetto, F., Del Sole, R., Cannoletta, D., Vasapollo, G. & Maffezzoli, A. Monitoring wood degradation during weathering by cellulose crystallinity. *Materials* **5**, 1910–1922 (2012).
 60. Xu, Y., Xu, Y. & Yue, X. Changes of hydrogen bonding and aggregation structure of cellulose fiber due to microwave-assisted alkali treatment and its impacts on the application as fluff pulp. *Cellulose* **24**, 967–976 (2017).
 61. Zhang, X., Huang, H., Qing, Y., Wang, H. & Li, X. A comparison study on the characteristics of nanofibrils isolated from fibers and parenchyma cells in bamboo. *Materials* **13**, (2020).
 62. Trilokesh, C. & Uppuluri, K. B. Isolation and characterization of cellulose nanocrystals from jackfruit peel. *Scientific Reports* **9**, 1–8 (2019).
 63. Fu, F. *et al.* Improved Synthesis of Cellulose Carbamates with Minimum Urea Based on an Easy Scale-up Method. *ACS Sustainable Chemistry and Engineering* **3**, 1510–1517 (2015).
 64. Costa, L. A. S. *et al.* Extraction and Characterization of Nanocellulose from Corn Stover. *Materials Today: Proceedings* **2**, 287–294 (2015).
 65. Kamińska, A. *et al.* Activated carbons obtained from orange peels, coffee grounds, and sunflower husks—Comparison of physicochemical properties and activity in the alpha-pinene isomerization process. *Materials* **14**, (2021).
 66. Kabenge, I. *et al.* Characterization of Banana Peels Wastes as Potential Slow Pyrolysis Feedstock. *Journal of Sustainable Development* **11**, 14 (2018).
 67. Goldstein, I. S. *Organic chemicals from biomass*. (CRC Press, 1981).
 68. Mohan, D., Pittman, C. U. & Steele, P. H. Pyrolysis of Wood/Biomass for Bio-oil: A Critical Review. *Energy & Fuels* **20**, 848–889 (2006).
 69. Carranza-Núñez, U. *et al.* Physicochemical characterization of natural fibers obtained from seed pods of *Ceiba aesculifolia*. *BioResources* **16**, 4200–4211 (2021).
 70. Yaradoddi, J. S. *et al.* Bio-based material from fruit waste of orange peel for industrial applications. *Journal of Materials Research and Technology* (2021) doi:10.1016/j.jmrt.2021.09.016.

71. Alcaraz, L. *et al.* Application of a low-cost cellulose-based bioadsorbent for the effective recovery of terbium ions from aqueous solutions. *Metals* **10**, 1–19 (2020).
72. Guerra, F. D., Campbell, M. L., Attia, M. F., Whitehead, D. C. & Alexis, F. Capture of Aldehyde VOCs Using a Series of Amine-Functionalized Cellulose Nanocrystals. *ChemistrySelect* **3**, 5495–5501 (2018).

Annexes

Annex A

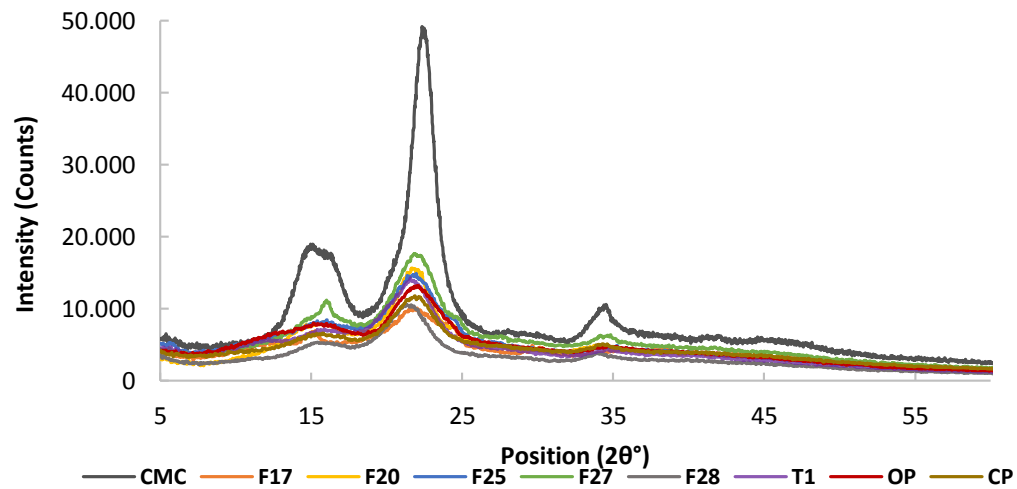


Figure 40. X-ray diffraction patterns graph comparison between samples extracted from natural sources and commercial cellulose (CMC).

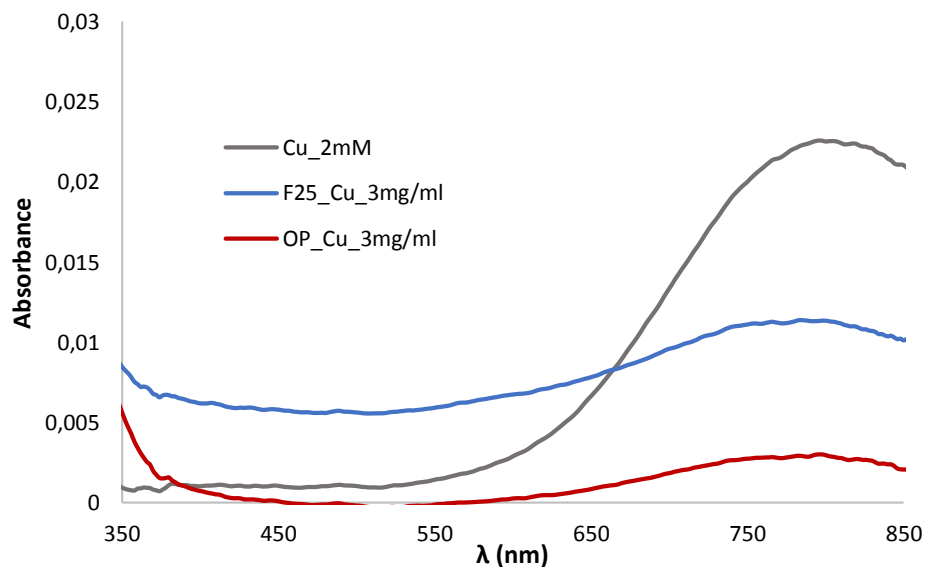


Figure 41. Uv-vis spectra after reaction C^{2+} ions (2mM) with the cellulose F25 and F25 using 3mg/ml

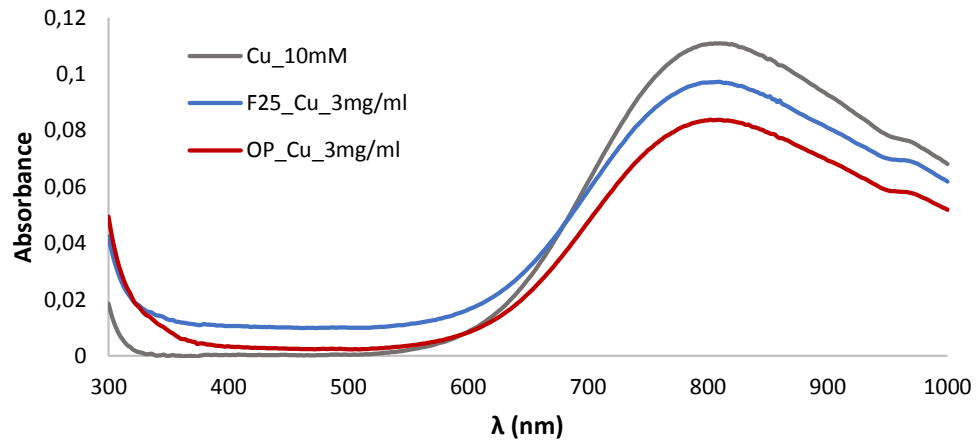


Figure 42. Uv-vis spectra after reaction Cu^{2+} ions (10mM) with the cellulose F25 and F25 using 3mg/ml

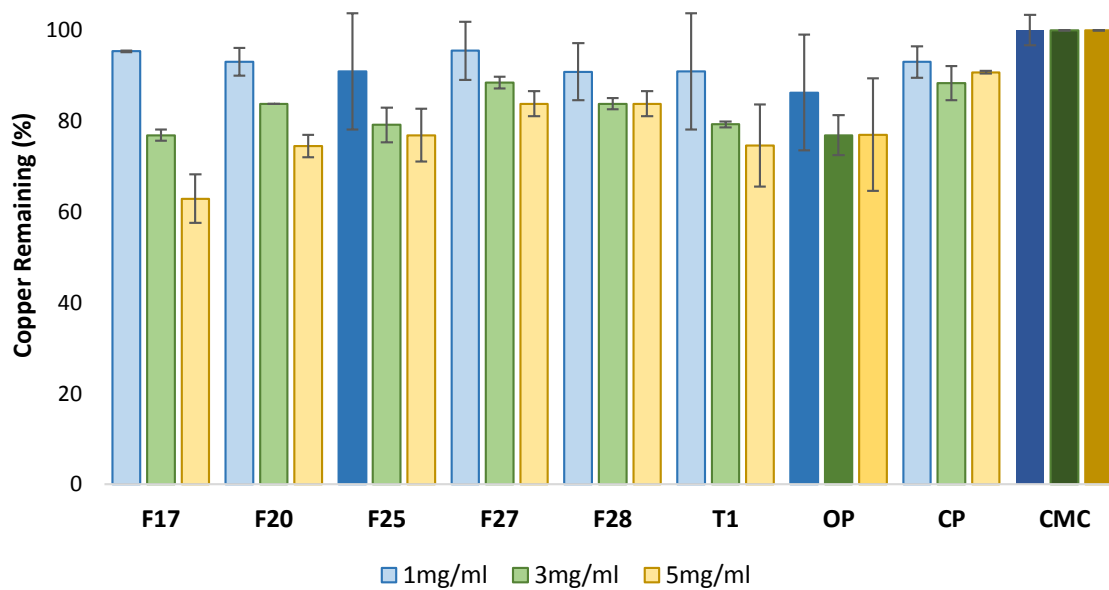


Figure 43. Percent of reduction of Cu^{2+} ions at low concentration (2mM), using the raw materials (without treatment).

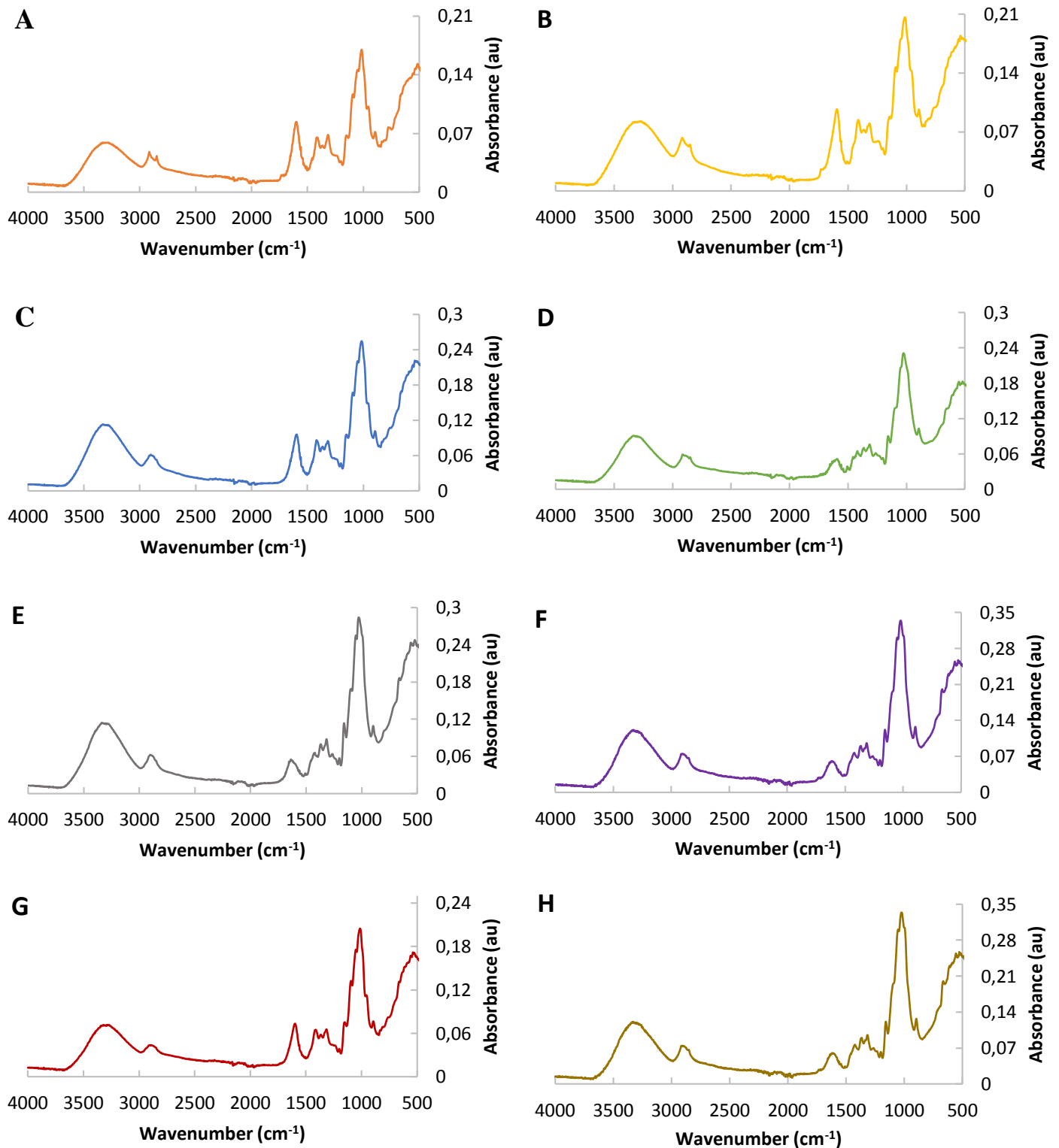


Figure 44. Fourier-transform infrared spectra of cellulose particles from natural sources: (A) F17, (B) F20, (C) F25, (D) F27, (E) F28, (F) T1, (G) OP, (H) CP.

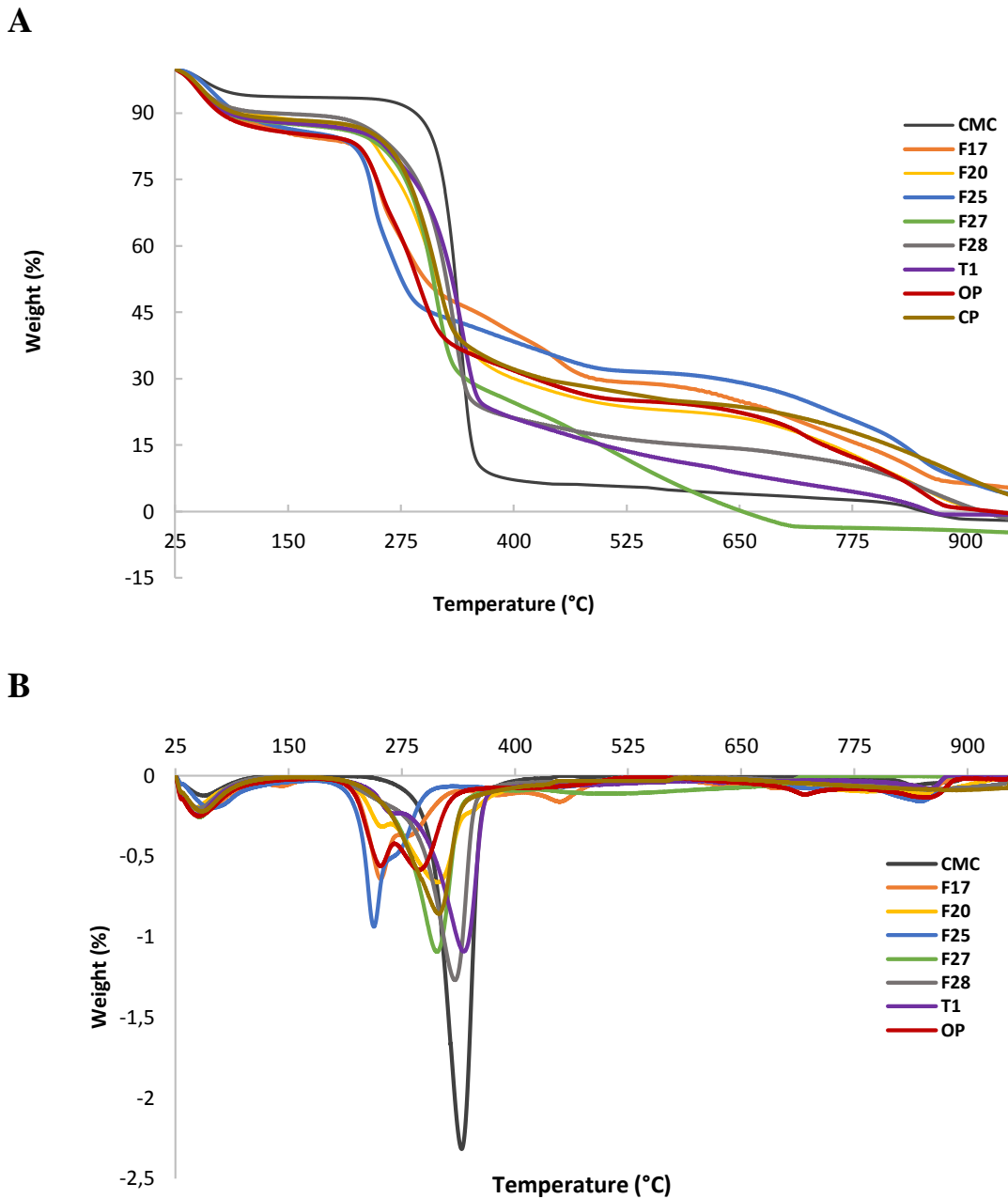


Figure 45. Thermogravimetry analysis profile of the (A) extracted cellulose, and the (B) peaks with the high weight loss.

Annex B

Table 11. Data of adsorption test using 1mg/ml.

1mg/ml						
2mM						
Samples	B0	B1	B2	mean	Standard Deviation	Cu Remaining (%)
F17	23,529	25,820	15,652	21,667	5,333	78,333
F20	23,529	28,689	27,391	26,536	2,684	73,464
F25	59,664	60,820	63,043	61,176	1,718	38,824
F27	19,328	23,361	16,087	19,592	3,644	80,408
F28	10,084	12,705	13,478	12,089	1,779	87,911
T1	15,966	20,697	20,870	19,178	2,782	80,822
OP	37,815	40,164	36,957	38,312	1,660	61,688
CP	11,765	24,590	21,739	23,165	2,016	76,835
CMC	-0,420	6,967	-3,043	1,168	5,191	98,832
10mM						
F17	11,419	11,960	14,750	12,710	1,788	87,290
F20	5,626	6,717	8,583	6,975	1,496	93,025
F25	15,281	14,535	14,750	14,855	0,384	85,145
F27	6,885	6,645	6,250	6,593	0,321	93,407
F28	4,282	6,229	5,750	5,420	1,015	94,580
T1	5,290	7,143	7,250	6,561	1,102	93,439
OP	12,091	13,040	13,167	12,766	0,588	87,234
CP	9,320	11,130	8,083	9,511	1,532	90,489
CMC	-1,175	-2,409	-0,750	-1,445	0,861	101,445

Table 12. Data of adsorption test using 3 mg/ml.

3mg/ml						
2mM						
Samples	B0	B1	B2	mean	Standard Deviation	Cu Remaining (%)
F17	29,41	31,56	43,04	34,67	7,33	65,33
F20	50,00	50,41	56,52	52,31	3,65	47,69
F25	64,71	64,34	61,30	63,45	1,87	36,55
F27	33,19	34,84	26,52	31,52	4,40	68,48
F28	26,89	30,33	28,70	28,64	1,72	71,36
T1	38,66	38,52	30,87	36,02	4,46	63,98
OP	69,33	67,21	71,96	69,50	2,38	30,50
CP	36,97	32,38	33,48	34,28	2,40	65,72
CMC	9,24	6,56	-8,26	2,51	9,43	97,49
10mM						
Samples	B0	B1	B2	mean	Standard Deviation	Cu Remaining (%)
F17	20,24	23,59	26,75	23,52	3,26	76,48
F20	10,08	15,37	15,75	13,73	3,17	86,27
F25	40,22	36,63	37,50	38,12	1,87	61,88
F27	10,41	9,63	9,75	9,93	0,42	90,07
F28	7,05	8,64	7,33	7,67	0,85	92,33
T1	7,14	12,04	11,08	10,09	2,60	89,91
OP	31,65	27,24	29,13	29,34	2,21	70,66
CP	100,00	13,54	13,83	13,69	0,21	86,31
CMC	1,26	2,66	-0,08	1,28	1,37	98,72

Table 13. Raw data of adsorption test using 5 mg/ml.

5mg/ml						
2mM						
Samples	B0	B1	B2	mean	Standard Deviation	Cu Remaining (%)
F17	51,26	52,87	53,48	52,54	1,15	47,46
F20	60,50	61,07	51,30	57,62	5,48	42,38
F25	91,60	87,70	86,96	88,75	2,49	11,25
F27	38,66	39,34	33,91	37,30	2,96	62,70
F28	33,61	40,98	30,00	34,87	5,60	65,13
T1	41,18	40,57	51,30	44,35	6,03	55,65
OP	89,08	89,75	86,52	88,45	1,70	11,55
CP	48,74	46,31	40,87	45,31	4,03	54,69
CMC	2,94	9,84	-4,35	2,81	7,09	97,19
10mM						
Samples	B0	B1	B2	mean	Standard Deviation	Cu Remaining (%)
F17	37,70	38,29	36,33	37,44	1,00	62,56
F20	18,81	21,01	17,33	19,05	1,85	80,95
F25	52,06	56,48	56,33	54,96	2,51	45,04
F27	8,98	10,80	10,75	10,18	1,03	89,82
F28	6,30	9,88	9,67	8,62	2,01	91,38
T1	12,01	16,03	15,08	14,37	2,10	85,63
OP	39,21	41,86	41,08	40,72	1,36	59,28
CP	14,02	15,45	15,67	15,05	0,89	84,95
CMC	-0,25	2,33	2,25	1,44	1,47	98,56

Table 14. Data of isotherms adsorption studies and fitting.

F25		Langmuir				Freundlich			
Ce (mg/L)	qe (mg/g)	1/Ce	1/qe	Lineal	Non Lineal	Log(Ce)	Log(qe)	Lineal	Non Lineal
37,490	28,864	0,0267	0,0346	28,8656	28,8593	1,5739	1,4604	31,1729	31,7722
142,463	36,684	0,0070	0,0273	36,3733	36,4106	2,1537	1,5645	34,3449	34,6990
266,931	36,647	0,0037	0,0273	38,0201	38,0695	2,4264	1,5640	35,9466	36,1673
644,833	40,549	0,0016	0,0247	39,2110	39,2696	2,8094	1,6080	38,3233	38,3353
832,284	42,289	0,0012	0,0236	39,4073	39,4675	2,9203	1,6262	39,0398	38,9865
1201,563	38,942	0,0008	0,0257	39,6171	39,6789	3,0797	1,5904	40,0944	39,9430
1475,242	37,994	0,0007	0,0263	39,7054	39,7680	3,1689	1,5797	40,6961	40,4876
1793,909	39,393	0,0006	0,0254	39,7746	39,8378	3,2538	1,5954	41,2780	41,0137
OP		Langmuir				Freundlich			
Ce (mg/L)	qe (mg/g)	1/Ce	1/qe	Lineal	Non Lineal	Log(Ce)	Log(qe)	Lineal	Non Lineal
11,622	39,375	0,0860	0,0254	39,0503	37,5548	1,0653	1,5952	40,8682	41,6035
100,849	55,546	0,0099	0,0180	58,3765	58,4786	2,0037	1,7447	51,0440	51,4452
213,507	52,107	0,0047	0,0192	60,4321	60,8071	2,3294	1,7169	55,1396	55,3803
459,631	62,893	0,0022	0,0159	61,4696	61,9902	2,6624	1,7986	59,6662	59,7143
570,227	61,043	0,0018	0,0164	61,6477	62,1938	2,7560	1,7856	61,0047	60,9930
767,613	62,768	0,0013	0,0159	61,8391	62,4129	2,8851	1,7977	62,8995	62,8009
1138,579	66,143	0,0009	0,0151	62,0204	62,6205	3,0564	1,8205	65,5037	65,2817
1414,508	64,204	0,0007	0,0156	62,0939	62,7047	3,1506	1,8076	66,9828	66,6887
1722,303	67,721	0,0006	0,0148	62,1482	62,7669	3,2361	1,8307	68,3536	67,9915

Annex C



Figure 46. Photographs taken during the research project.